Liang, Y., Lancaster, F. and Izzuddin, B.A. (2016) Effective modelling of structural glass with laminated shell elements. Composite Structures, 156, pp. 47-62.

http://eprints.gla.ac.uk/186394/

Deposited on: 10 May 2019

Effective Modelling of Structural Glass with Laminated Shell Elements

Y. Liang[1], F. Lancaster[2], B.A. Izzuddin[3]

Abstract

The cross-sectional behaviour of laminated glass (LG) is characterised by a significant zigzag effect owing to the large stiffness mismatch between the glass and polymer layers. The approach incorporated in current glass design standards is based on the use of a monolithic model with an effective thickness, which suffers several sources of inaccuracy and limitations. In this paper, laminated shell elements with an alternating stiff/soft lay-up are enhanced and used to model LG structures, so as to accurately reproduce the through-thickness behaviour of LG with a minimal number of zigzag displacement parameters per node. In order to consider the influence of loading rate and temperature on the response of LG, a linear viscoelastic material model is adopted to simulate the polymer interlayer, which is formulated based on a recursive formula for stress calculation. Finally, several applications of the proposed modelling approach for two-ply and multi-ply LG structures are presented, considering typical deflection, stability and creep problems, where the benefits of the proposed approach are demonstrated through comparisons against monolithic shell models based on an effective thickness as well as 3D continuum models.

Keywords: laminated glass; viscoelastic material; effective thickness; zigzag effect; transverse shear strain.

---

[1] Research student, Department of Civil and Environmental Engineering, Imperial College London SW7 2AZ.

[2] Eckersley O'Callaghan, 137 Varick Street, #406, New York, NY 10013, (franklin@eocengineers.com).

[3] Professor of Computational Structural Mechanics, Department of Civil and Environmental Engineering, Imperial College London, SW7 2AZ, (Corresponding author, b.izzuddin@imperial.ac.uk).

1   INTRODUCTION

Laminated glass (LG) has been widely used in many applications of structural engineering owing to its transparency, aesthetic appearance and safety characteristics. It is composed of two or more glass plies bonded by polymer layers. Polyvinyl butyral (PVB) is the most commonly used interlayer, which, in the event of fracture of glass plies, could mitigate injury to occupants by retaining glass debris in place, withstanding further loadings, and absorbing more energy. In the previous century, LG has been mainly used as secondary structural components, such as façades in high-rise buildings, due to the brittle material characteristic of glass. More recently with the development of new interlayer materials [1-2] and improvements in glass manufacture, the utilisation of LG has also been extended to fundamental load resisting systems in some glass structures (e.g., roofs, stairs, beams and columns) [3].

Despite the universally increasing interest in LG structures, there is a lack of adequate design and assessment guidance for such structures. The use of a monolithic model with an 'effective thickness' has been suggested for the simplified analysis of LG in several design codes, including the American standard ASTM E1300 12-a [4] and the preliminary version of European standard prEN 13474 [5]. The fundamental idea of such approaches is to establish an effective monolithic thickness based on the material, geometry, and loading conditions of the considered LG beam, and to use a monolithic plate/shell model with this effective thickness and the same loading and boundary conditions for the prediction of the maximum deflection or stresses in the glass plies. Although the shear transfer capacity of the PVB interlayer is considered in the effective thickness approaches, their accuracy depends on the considered geometry and loading and boundary conditions [6-7].

For an efficient design of LG structures, laminated shell models are actually more suitable than monolithic shell models owing to their ability to incorporate through-thickness descriptions of displacements and stresses, and pose much more realistic computational demands compared to three-dimensional (3D) continuum models while maintaining good levels of accuracy. Considerable research efforts have been devoted to the establishment of plate theory-based lamination models for a close estimation of the structural behaviour at

reduced computational demands. Layer-wise models (LWMs) pioneered by Reddy and co-workers [8-10] achieve the reproduction of piecewise continuous displacement fields in the thickness direction by employing first-order shear deformation theory (FSDT) or higher-order shear deformation theories (HSDTs) at each constitutive layer. On the other hand, equivalent single layer models (ESLMs) [11-16] obtain piecewise displacements by simply adding Murakami's zigzag function [11] to a classical Taylor type expansion defined along the whole plate thickness. Both the LWMs and the ESLMs have shown good agreement with the 3D continuum models, which thus have been widely used for simulating laminated plates and shells.

In order to predict well the response of LG prior to fracture, the laminated shell models should cover the following mechanical characteristics:

(i) Material mismatch. There is a significant stiffness variation through the thickness of LG where the glass-to-PVB stiffness ratio falls into the range from 10^3 to 10^6, which leads to a significant zigzag effect in displacements and complex stress fields in the thickness direction.

(ii) Stacking sequence. The LG is associated with an alternating stiff/soft lay-up, which differs from usually encountered sandwich structures where all soft cores are layered together and sandwiched by outer stiff sheets.

(iii) Large slenderness. Most LG components can be regarded as two-dimensional (2D) structures, which induce large deflections under transverse loading, and which are prone to structural instability under planar loading.

(iv) Sensitivity to loading duration and temperature. The PVB interlayer is a viscoelastic material, the mechanical properties of which vary with different loading rates and temperature, hence leading to varying effective sectional modulus of the glass laminate [17].

Recently, triangular and quadrilateral laminated shell elements have been developed by the authors [18-19], both of which fulfil the requirements (i)-(iii). In the embedded lamination model, zigzag displacements and transverse shear strain distributions following an alternating stiff/soft lay-up with very large stiffness ratio, as encountered in LG, were

proposed [18]. In order to eliminate locking phenomena which arise with conforming displacement-based shell elements, the Mixed Interpolation of Tensorial Components (MITC) method [20-22] was employed, which overcomes locking by offering a two-level approximation that samples and interpolates strain components in a covariant coordinate system at a selection of positions. The application of the MITC method to each constitutive layer of the 6-noded and 9-noded laminated shell elements has been shown to yield improved element performance [18-19]. Furthermore, a co-rotational approach has been developed [23-24] and adopted for geometric nonlinear analysis of the laminated shell elements, allowing the consideration of large displacement and buckling analysis.

In this paper, an overview of the proposed approach for modelling LG using laminated shell element is provided, highlighting the limitations of the current monolithic approach in view of the through-thickness behaviour of LG, and presenting the relevant features of the developed laminated shell elements. A linear viscoelastic material model [25], adapted to laminated shell elements, is then presented to consider the influence of temperature and the loading rate on the interlayer mechanical properties. By using suitable material models and properties for glass and PVB, the proposed modelling approach utilising triangular and quadrilateral laminated shell elements can be applied for the accurate and efficient nonlinear analysis of a wide range of LG structural problems. This is demonstrated in this paper through several application examples of two-ply and multi-ply LG structures, considering typical deflection, stability and creep problems, where the benefits of the proposed approach compared to the monolithic effective thickness approach as well as 3D continuum models are clearly demonstrated.

2   LIMITATION OF CURRENT EFFECTIVE THICKNESS APPROACH

In current LG design codes, the effective thickness approach is usually suggested for the estimation of the maximum deflection and stresses in glass members. This approach aims at replacing a LG member with a monolithic glass member of the same planar dimensions, subject to the same loading and boundary conditions, except for the member thickness, such that the predicted maximum deflection or stress offers an adequate approximation of the

corresponding entity in the real LG member. Accordingly, this effective thickness approach allows in principle the use of simple monolithic shell elements in the finite element (FE) model.

2.1 The effective thickness approach in ASTM E1300-12a

Appendix X9 of ASTM E1300-12a [4] provides engineering formulae for calculating the effective thickness of LG. Two different effective thickness values are determined for the prediction of the maximum deflection and the maximum stress in glass ply, respectively. These effective thickness values can be used with standard engineering formulae or FE methods for deriving both the deflection and stress of glass plies.

In order to consider the influence of the shear transfer capacity of PVB on the overall structural behaviour of LG, a coefficient, Γ, is defined as a measure of the transfer of shear stresses across the interlayer [4]:

$$\Gamma = \frac{1}{1 + 9.6 \dfrac{EI_s h_v}{Gh_s^2 a^2}} \tag{1}$$

with:

$$I_s = h_1 h_{s,2}^2 + h_2 h_{s,1}^2 \tag{2}$$

$$h_{s,1} = \frac{h_s h_1}{h_1 + h_2}, \quad h_{s,2} = \frac{h_s h_2}{h_1 + h_2} \tag{3}$$

$$h_s = 0.5(h_1 + h_2) + h_v \tag{4}$$

where h_v is the interlayer thickness; h_1 and h_2 are the minimum thicknesses of the two glass plies; E is glass Young's modulus; a is the smallest in-plane dimension of bending of the laminate plate; and G is the interlayer complex shear modulus.

For calculations of the maximum deflection, the effective thickness of the two-ply LG is given as [4]:

$$h_{ef,w} = \sqrt[3]{h_1^3 + h_2^3 + 12\Gamma I_s} \tag{5}$$

For calculations of the maximum glass bending stresses in glass plies '1' and '2', the corresponding effective thicknesses of the two-ply LG are given as [4]:

$$h_{1,ef,\sigma} = \sqrt{\frac{h_{ef,w}^3}{h_1 + 2\Gamma h_{s,2}}}, \quad h_{2,ef,\sigma} = \sqrt{\frac{h_{ef,w}^3}{h_2 + 2\Gamma h_{s,1}}} \tag{6}$$

It is important to note that the above formulation is based on the original approach by Wölfel [26], who proposed a simple method to calculate the effective thickness of a monolithic beam with equivalent bending properties to a sandwich composite beam. It was assumed that (i) the external face sheets are thin enough to ignore the bending stiffness, and (ii) the interlayer resists shear force only. Later, Bennison et al. [27-28] developed Wölfel's method specifically for the application to LG. The shear transfer coefficient, Γ, was defined by a universal expression:

$$\Gamma = \frac{1}{1 + \beta \dfrac{EI_s h_v}{Gh_s^2 a^2}} \tag{7}$$

where β is a coefficient depending on the loading condition. For uniform loading, $\beta = 9.6$, which was adopted by ASTM E1300-12a, as shown in (1). Bennison et al. [27-28] also proposed an approximate second moment of area of the cross-section, which includes the contribution from the bending stiffness of the face sheets. In addition, it was assumed in the model that the shear force was resisted by the core layer only.

Galuppi and Royer-Carfagni [6-7] noted that the effective thickness approach in ASTM E1300-12a is accurate only for simply-supported beams under uniformly distributed loading and in those cases where the deflected shape is similar to this reference case. For other loading cases and for LG plates and shells, the above formula may not capture the structural response well. It is also noted that this approach could determine the effective thickness for beams and rectangular plates only. For LG members with other geometry, such as circular LG plates, the effective thickness cannot be determined by this approach.

2.2 Cumulative effective thickness approach for multi-ply laminated glass

The aforementioned effective thickness method is applicable to two-ply LG. For multi-ply LG, the displacement-effective thickness can in principle be easily obtained incrementally. The effective thickness of the first and second glass plies is calculated firstly, and then the

corresponding equivalent monolith is combined with the third glass ply to calculate a new effective thickness. The same step is repeated until an effective thickness for the entire lamination is derived. This cumulative effective thickness approach has been suggested in a preliminary version of the European Standard prEN 13474 [5] and was described by Zenkert et al. [29].

However, it has been pointed out by Galuppi and Royer-Carfagni that for the cases where the glass plies or the interlayers are not all of the same thickness, different effective thicknesses may be obtained depending on the chosen sequence of layers [7]. Another drawback of the generalised formula is that the effective thickness definition for maximum ply stresses is quite ambiguous, and the stress-effective thicknesses for internal layers can never be calculated [7].

Therefore, the use of monolithic shell elements for the analysis of general multi-ply LG structures is fraught with inaccuracy and inapplicability. As an alternative, laminated shell elements offer a realistic option, combining accuracy and efficiency in the FE modelling of LG structures, provided the through-thickness behaviour of LG is captured well.

3 THROUGH-THICKNESS BEHAVIOUR OF LAMINATED GLASS

Herein, a simply-supported LG beam under a concentrated force at the mid-span is considered for illustration purposes (Figure 1), where a unit width is assumed and a 2D plane stress analysis is performed. Isotropic material models are used for both glass and PVB. Two LG lay-ups and two sets of material properties for the PVB interlayer are considered, resulting in four cases as follows:

Case 1: two-ply LG with long-duration material properties of PVB;

Case 2: two-ply LG with short-duration material properties of PVB;

Case 3: four-ply LG with long-duration material properties of PVB;

Case 4: four-ply LG with short-duration material properties of PVB.

The geometric and material parameters, and the loading and boundary conditions are listed in Table 1.

The through-thickness distributions of the quarter-span (x=L/4) longitudinal displacement by the 2D analysis are depicted in Figure 2, represented by dash lines with crosses. Evident from the graphs, significant zigzag effect is observed for Cases 1 and 3, corresponding to the long-duration material properties of PVB. On the other hand, for Cases 2 and 4 the cross-sectional warping is less significant owing to the higher shear transfer capacity of PVB for short-duration loading. Table 2 lists the predicted rotations of the layer normals by 2D analysis for all the considered cases, from which it is found that the normals of all glass plies rotate by a nearly identical value for all the considered cases.

Table 3 lists the percentage contribution of each layer to the overall transverse shear strain energy for all considered cases. It is observed that, compared with glass plies, the PVB interlayers contribute more to the overall transverse shear strain energy. Provided that the transverse shear strain distribution of the PVB interlayers is accurately represented, a good estimation of the overall transverse shear strain energy can be obtained. Figure 3 depicts the through-thickness distributions of the transverse shear strain by 2D analysis, represented by dash lines with crosses.

Therefore, the through-thickness behaviour of LG under transverse loading is characterised by two features that distinguish it from other laminations: on one hand, all the glass plies exhibit nearly the same rotations of their ply normals; on the other hand, transverse shear strain energy comes mainly from the flexible PVB, with the transverse shear strain exhibiting a near constant variation in each PVB interlayer. Provided that a lamination model captures both characteristics, an accurate representation of the through-thickness behaviour of LG members can be obtained.

4 LAMINATED SHELL ELEMENT WITH AN ALTERNATING STIFF/SOFT LAY-UP

Two efficient geometrically nonlinear laminated shell elements, Ln-MITC6 and Ln-MITC9, have been recently developed for the analysis of laminations with an alternating stiff/soft lay-up [18-19], where 'L' stands for 'layer', n is the number of layers, and 'MITC6' and 'MITC9' stands for the employment of an MITC6 and an MITC9 strain mapping approach for overcoming locking in the curved triangular and quadrilateral elements. In both

element formulations, displacement fields and transverse shear strain fields have been assumed in accordance with the aforementioned characteristics. In the following, the elements Ln-MITC6 and Ln-MITC9 are briefly described.

4.1 Co-rotational system

In formulating large displacement finite elements for small-strain problems, the relationship between the strain and displacement fields is highly nonlinear and complex if the displacement fields are referred to a fixed coordinate system, where the nonlinear strain terms arise mainly from the element rigid body rotations. In this respect, both the Ln-MITC6 and the Ln-MITC9 elements employ the co-rotational approach [23-24] to overcome this complexity. The coordinates of the corner nodes are used to define the co-rotational coordinate system that follows the element current configuration throughout the analysis, which addresses geometric nonlinearity through transformations between the local and global systems that are applied at the level of discrete element parameters, hence enabling the use of a low-order strain displacement relationship at the local element level.

Assuming shallow shell elements, the local x- and y-axes are located at the middle surface of the lamination, while the z-axis is normal to the element plane (as shown in Figure 4). Each layer is identified by a unique index and is numbered from the bottom of the lamination, with N_l denoting the total number of layers.

4.2 Through-thickness description of displacements

The Ln-MITC6 and Ln-MITC9 elements with an alternating stiff/soft lay-up assume that the variation of planar displacements through its thickness is of a piecewise linear pattern, and that all stiff sheets have identical rotations of the normal whereas the soft sheets allow different rotations. Accordingly, for a LG consisting of (N_c+1) glass plies bonded by N_c interlayers (the subscript 'c' denotes the soft interlayer), the through-thickness distribution of the planar displacements can be decomposed into a constant and a linear mode, in accordance with the Reissner-Mindlin kinematic hypothesis, as well as N_c zigzag modes, denoted by $\Lambda_j(z)$ $(j = 1 \rightarrow N_c)$, which are orthogonal to the constant and linear modes and associated

with the change of normals in the soft PVB layers [18]. The zigzag modes $\Lambda_j(z)$ for a three-ply LG are depicted in Figure 5 for an illustration.

The resulting planar displacement fields are expressed as [18]:

$$u_\alpha(x,y,z) = u_{\alpha 0}(x,y) + z\theta_\alpha(x,y) + \sum_{j=1}^{N_c} \Lambda_j(z)\vartheta_\alpha^j(x,y) \qquad (\alpha = x,y) \qquad (8)$$

where $u_{\alpha 0}$ are the planar displacement fields along the x- or y-axis evaluated on the middle surface, θ_α are the components of the normal vector along the x- or y-axis in the absence of zigzag displacements, and ϑ_α^j are the additional fields associated with the proposed zigzag functions along the x- or y-axis.

The transverse displacement is assumed to be constant through the plate thickness, and is thus denoted by $u_{z0}(x,y)$. It is worth noting that in order to eliminate the nonlinear co-rotational transformations of forces and stiffness associated with the zigzag parameters a 2D shell system was proposed to define the additional zigzag parameters directly [18, 30].

In accordance with the assumed displacement fields, $(5+2N_c)$ displacement parameters are defined for each node, resulting in a vector of local displacement parameters $\mathbf{U}_C$ and a vector of additional zigzag displacement parameters $\mathbf{U}_A$ for the laminated shell elements:

$$\mathbf{U}_C = \left\langle \mathbf{U}_{C1}^T, \cdots, \mathbf{U}_{Ci}^T, \cdots, \mathbf{U}_{CN_e}^T \right\rangle^T, \quad \mathbf{U}_{Ci} = \left\langle u_{x0,i}, u_{y0,i}, u_{z0,i}, \theta_{x,i}, \theta_{y,i} \right\rangle^T \qquad (9)$$

$$\mathbf{U}_A = \left\langle \mathbf{U}_{A1}^T, \cdots, \mathbf{U}_{Ai}^T, \cdots, \mathbf{U}_{AN_e}^T \right\rangle^T, \quad \mathbf{U}_{Ai} = \left\langle \vartheta_{x,i}^1, \vartheta_{y,i}^1, \cdots, \vartheta_{x,i}^{N_c}, \vartheta_{y,i}^{N_c} \right\rangle^T \qquad (10)$$

where N_e is the number of nodes for the considered element (6 for the triangular element and 9 for the quadrilateral element), with *i* referring to the node number.

4.3 Kinematics of constitutive layer

Each constitutive layer of the lamination shell element is regarded as a pseudo Reissner-Mindlin plate, with the translational displacements $\left(u_x^{(k)}, u_y^{(k)}, u_z^{(k)}\right)$ and rotations $\left(\theta_x^{(k)}, \theta_y^{(k)}\right)$ on the layer mid-surface obtained from the employed description of displacement fields, resulting in the following relationship [18]:

$$u_\alpha^{(k)} = u_{\alpha 0} + z^{(k)}\theta_\alpha + \sum_{j=1}^{N_c} \Lambda_j^{(k)}\vartheta_\alpha^j \qquad (\alpha = x,y) \qquad (11)$$

$$u_z^{(k)} = u_{z0} \tag{12}$$

$$\theta_\alpha^{(k)} = \left.\frac{\partial u_\alpha^{(k)}}{\partial z}\right|_{z^{(k)}} = \theta_\alpha + \sum_{j=1}^{N_c} \lambda_j^{(k)} \vartheta_\alpha^j, \quad \lambda_j^{(k)} = \left.\frac{\partial \Lambda_j}{\partial z}\right|_{z^{(k)}} \qquad (\alpha = x, y) \tag{13}$$

where $\Lambda_j^{(k)} \equiv \Lambda_j(z^{(k)})$ represents the extracted value of the zigzag function $\Lambda_j(z)$ on the middle surface of layer (k); $z^{(k)}$ is the extracted value of z on the middle surface of layer (k).

Accordingly, the relationship between the nodal parameters and the pseudo nodal parameters at layer (k) is expressed as [18]:

$$\mathbf{U}^{(k)} = \mathbf{T}_C^{(k)} \mathbf{U}_C + \mathbf{T}_A^{(k)} \mathbf{U}_A \tag{14}$$

where: $\mathbf{U}_C$ and $\mathbf{U}_A$ are local nodal parameters and additional parameters, respectively; $\mathbf{T}_C^{(k)}$ and $\mathbf{T}_A^{(k)}$ are the transformation matrices; and $\mathbf{U}^{(k)}$ are the pseudo nodal parameters at layer (k), expressed as:

$$\mathbf{U}^{(k)} = \left\langle \mathbf{U}_1^{(k)T}, \cdots, \mathbf{U}_i^{(k)T}, \cdots, \mathbf{U}_{N_e}^{(k)T} \right\rangle^T, \quad \mathbf{U}_i^{(k)} = \left\langle u_{x,i}^{(k)}, u_{y,i}^{(k)}, u_{z,i}^{(k)}, \theta_{x,i}^{(k)}, \theta_{y,i}^{(k)} \right\rangle^T \tag{15}$$

The layer displacement fields $\left(u_x^{(k)}, u_y^{(k)}, u_z^{(k)}, \theta_x^{(k)}, \theta_y^{(k)} \right)$ are obtained by interpolating the pseudo nodal parameters with shape functions. For the 9-noded quadrilateral element, the shape functions are expressed in terms of natural coordinates (ξ, η) as follows:

$$N_i(\xi, \eta) = \frac{(\xi - \xi_i{}')(\xi - \xi_i{}'')}{(\xi_i - \xi_i{}')(\xi_i - \xi_i{}'')} \cdot \frac{(\eta - \eta_i{}')(\eta - \eta_i{}'')}{(\eta_i - \eta_i{}')(\eta_i - \eta_i{}'')} \quad (i = 1 \to 9) \tag{16}$$

where (ξ_i, η_i) represent the natural coordinates of node i, $(\xi_i \neq \xi_i{}' \neq \xi_i{}'') = -1, 0, 1$ and $(\eta_i \neq \eta_i{}' \neq \eta_i{}'') = -1, 0, 1$.

For the 6-noded triangular element, the shape functions are expressed in terms of area coordinates (L_1, L_2, L_3) as follows:

$$N_i = L_i(2L_i - 1), \quad N_{i+3} = 4L_i L_{i+} \quad (i = 1 \to 3) \tag{17}$$

where $i_+ = \mod(i, 3) + 1$, and (L_1, L_2, L_3) are the area coordinates, with $L_1 = 1 - \xi - \eta$, $L_2 = \xi$, and $L_3 = \eta$.

In the local element system, the strain state within each layer (k) is fully determined by the membrane strains $\boldsymbol{\varepsilon}_m^{(k)}$, bending generalised strains $\boldsymbol{\varepsilon}_b^{(k)}$, and transverse shear strains $\boldsymbol{\varepsilon}_s^{(k)}$, which are obtained as follows [18]:

$$
\boldsymbol{\varepsilon}_m^{(k)} = \left\{ \begin{array}{c} \varepsilon_x^{(k)} \\[2mm] \varepsilon_y^{(k)} \\[2mm] \gamma_{xy}^{(k)} \end{array} \right\} = \left\{ \begin{array}{c} \dfrac{\partial u_x^{(k)}}{\partial x} \\[3mm] \dfrac{\partial u_y^{(k)}}{\partial y} \\[3mm] \dfrac{\partial u_x^{(k)}}{\partial y} + \dfrac{\partial u_y^{(k)}}{\partial x} \end{array} \right\} + \left\{ \begin{array}{c} \dfrac{1}{2}\left(\dfrac{\partial z_0}{\partial x} + \dfrac{\partial u_z^{(k)}}{\partial x} \right)^2 - \dfrac{1}{2}\left(\dfrac{\partial z_0}{\partial x} \right)^2 \\[4mm] \dfrac{1}{2}\left(\dfrac{\partial z_0}{\partial y} + \dfrac{\partial u_z^{(k)}}{\partial y} \right)^2 - \dfrac{1}{2}\left(\dfrac{\partial z_0}{\partial y} \right)^2 \\[4mm] \left(\dfrac{\partial z_0}{\partial x} + \dfrac{\partial u_z^{(k)}}{\partial x} \right)\left(\dfrac{\partial z_0}{\partial y} + \dfrac{\partial u_z^{(k)}}{\partial y} \right) - \left(\dfrac{\partial z_0}{\partial x} \right)\left(\dfrac{\partial z_0}{\partial y} \right) \end{array} \right\}
\tag{18}
$$

$$
\boldsymbol{\varepsilon}_b^{(k)} = \left\{ \begin{array}{c} \kappa_x^{(k)} \\[2mm] \kappa_y^{(k)} \\[2mm] \kappa_{xy}^{(k)} \end{array} \right\} = \left\{ \begin{array}{c} \dfrac{\partial \theta_x^{(k)}}{\partial x} \\[3mm] \dfrac{\partial \theta_y^{(k)}}{\partial y} \\[3mm] \dfrac{\partial \theta_x^{(k)}}{\partial y} + \dfrac{\partial \theta_y^{(k)}}{\partial x} \end{array} \right\}
\tag{19}
$$

$$
\boldsymbol{\varepsilon}_s^{(k)} = \left\{ \begin{array}{c} \gamma_{xz}^{(k)} \\[2mm] \gamma_{yz}^{(k)} \end{array} \right\} = \left\{ \begin{array}{c} \theta_x^{(k)} + \dfrac{\partial u_z^{(k)}}{\partial x} \\[3mm] \theta_y^{(k)} + \dfrac{\partial u_z^{(k)}}{\partial y} \end{array} \right\}
\tag{20}
$$

in which z_0 represents the offset of the shell mid-surface along the z-axis of the element local system. It is worth noting that quadratic terms of the membrane strains in (18) are not necessary within a co-rotational approach but enable better accuracy with coarser meshes.

In order to address the locking phenomenon in the 6-noded and 9-noded shell elements, the MITC6 [20] and MITC9 [21-22] strain-mapping approaches are employed in the local formulation of each constitutive layer [18-19].

4.4 Through-thickness description of transverse shear

In both the Ln-MITC6 and the Ln-MITC9 formulations, a through-thickness distribution of the transverse shear strain is assumed as follows [18]:

$$
\boldsymbol{\varepsilon}_{s,AS}^{(k)} = \omega^{(k)} F_k(z) \boldsymbol{\varepsilon}_s^{(k)} \quad z \in \left[h_{k-}, h_{k+} \right]
\tag{21}
$$

$$
F_1(z) = 1 + \frac{2\left(z - z^{(1)} \right)}{h_1}, \quad F_{N_1}(z) = 1 - \frac{2\left(z - z^{(N_1)} \right)}{h_{N_1}}, \quad F_k(z) = 1 \ (k = 2 \rightarrow N_1 - 1)
\tag{22}
$$

where $\omega^{(k)}$ is the shear correction factor of layer (k), which can be derived from energy equivalence at the generalised stress/strain and material stress/strain levels, resulting in $\omega^{(1)} = \omega^{(N_1)} = \dfrac{3}{4}$ and $\omega^{(k)} = 1$ $(k = 2 \rightarrow N_1 - 1)$.

In the range of the glass-to-PVB stiffness ratios, this assumed distribution for the transverse shear strain offers a realistic representation of the exact solution, albeit with discontinuous transvers shear stresses. This is besides the fact that an assumed strain distribution is much more practical than an assumed stress distribution when considering material nonlinearity. The exclusion of stress coupling between layers leads to a lamination formulation that achieves good levels of accuracy with high computational efficiency, which becomes even more pronounced for multi-ply LG.

The considered LG beam problem in Section 3 is also analysed with a mesh of laminated beam elements employing the aforementioned through-thickness description of displacements and transverse shear strain, with sufficient elements considered to provide a convergent solution. The through-thickness distributions of displacements and transverse shear strains by the lamination models are depicted in Figures 2 and 3, respectively, represented by dotted lines with circles. The predicted layer rotations and transverse shear strain portions by the lamination models are listed in Tables 4 and 5, respectively. The results of the lamination models, in comparison with the solution by 2D analysis, show excellent accuracy with a minimal number of additional parameters and a decoupled relationship of the transverse shear stress at laminar interfaces.

The efficiency and effectiveness of the 6-noded and 9-noded laminated shell elements Ln-MITC6 and Ln-MITC9 have been verified elsewhere [18-19]. In this paper, both elements are employed for the FE modelling of LG structures with different number of glass plies, various geometric configurations and subject to different loading conditions.

5   LINEAR VISCOELASTIC MATERIAL MODEL

PVB is a viscoelastic material, the mechanical properties of which depend on the temperature and the loading duration. For a reference temperature T_0, the viscoelastic

material property can be described by a generalised Maxwell model, which is expressed as a Prony series [17, 31]:

$$E(t) = E_\infty + \sum_{j=1}^{N_M} E_j e^{-t/\tau_j} \tag{23}$$

where N_M is the number of Maxwell elements employed in the Maxwell series; τ_j is a relaxation time parameter of the jth Maxwell element; E_∞ is the long-time plateau modulus.

The time-temperature correspondence principle states that the effect of changing temperature is the same as applying a multiplicative factor to the time scale, which can be expressed as follows [32] :

$$E(T, t) = E(T_0, t/a_T) \tag{24}$$

where T is an arbitrary temperature, t is the real time scale, and the coefficient a_T can be obtained with the use of the Williams-Landell-Ferry (WLF) equation [33]:

$$\log_{10} a_T = -\frac{C_1(T - T_0)}{C_2 + T - T_0} \tag{25}$$

in which C_1 and C_2 are constants that vary from polymer to polymer.

Equation (24) states that if the material modulus-time curve at a reference temperature T_0 is known, the modulus-time curve at an arbitrary temperature T can be obtained from the known curve by multiplying the time scale with a factor $1/a_T$.

The Boltzmann superposition principle yields a stress-strain relationship given as [32]:

$$\sigma(t) = \int_0^t E(t - s) \frac{\partial \varepsilon(s)}{\partial s} ds \tag{26}$$

The substitution of (23) into (26) leads to the following expression for the stress relaxation:

$$\sigma(t) = \int_0^t E_\infty \frac{\partial \varepsilon(s)}{\partial s} ds + \sum_{j=1}^{N_M} \int_0^t E_j e^{-\frac{t-s}{\tau_j}} \frac{\partial \varepsilon(s)}{\partial s} ds = E_\infty \varepsilon(t) + \sum_{j=1}^{N_M} H_j(t) \tag{27}$$

where H_j are history stress terms.

A recursive formula for the calculation of stress relaxation [25] is employed and adapted herein for the simulation of the PVB interlayer.

5.1 Recursive formula for stress relaxation

Temporal discretisation of (27) leads to the stress relaxations at the previous time t_n and the current time t_{n+1}:

$$\sigma^n = E_\infty \, \varepsilon^n + \sum_{j=1}^{N_M} H_j^n \tag{28}$$

$$\sigma^{n+1} = E_\infty \, \varepsilon^{n+1} + \sum_{j=1}^{N_M} H_j^{n+1} \tag{29}$$

In order to obtain a recursive formula for the stress, Sedef et al. [25] assumed a linear strain variation in the current time step $\Delta t^{n+1} = t_{n+1} - t_n$:

$$\frac{\partial \varepsilon(s)}{\partial s} = \frac{\varepsilon^{n+1} - \varepsilon^n}{\Delta t^{n+1}} \tag{30}$$

Accordingly, the history stress terms at the current time step, H_j^{n+1}, are related to H_j^n of the previous time step with the following relationship:

$$H_j^{n+1} = e^{-\frac{\Delta t^{n+1}}{\tau_j}} H_j^n + E_j \left(\int_{t_n}^{t_{n+1}} e^{-\frac{t_{n+1}-s}{\tau_j}} ds \right) \left(\frac{\Delta \varepsilon^{n+1}}{\Delta t^{n+1}} \right) \tag{31}$$

where $\Delta \varepsilon^{n+1} = \varepsilon^{n+1} - \varepsilon^n$.

Further integration of (31) leads to:

$$H_j^{n+1} = e^{-\frac{\Delta t^{n+1}}{\tau_j}} H_j^n + E_j A_j \Delta \varepsilon^{n+1} \tag{32}$$

with:

$$A_j = \frac{1 - e^{-\frac{\Delta t^{n+1}}{\tau_j}}}{\frac{\Delta t^{n+1}}{\tau_j}} \tag{33}$$

Substitution of (32) into (29) thus leads to a recursive formula for stress relaxation.

5.2 Application to interlayer material

Bennison et al. [31] conducted hydrostatic volumetric tests on PVB at different temperatures, and found that the value of the bulk modulus K(t) was relatively unchanged

with temperature, which was fixed at around 2.0GPa. Accordingly, it is assumed herein that the bulk modulus, K, of the interlayer material has a constant value whereas the shear relaxation function, G(t), can be expressed as a generalised Maxwell series. Then the stress relaxation is derived as follows:

$$\sigma_{ii}(t) = \int_0^t G(t-s)\left(\frac{4}{3}\frac{\partial \varepsilon_{ii}}{\partial s} - \frac{2}{3}\frac{\partial \varepsilon_{i_+ i_+}}{\partial s} - \frac{2}{3}\frac{\partial \varepsilon_{i_- i_-}}{\partial s}\right)ds + K\left[\varepsilon_{ii}(t) + \varepsilon_{i_+ i_+}(t) + \varepsilon_{i_- i_-}(t)\right] \tag{34}$$

$$\sigma_{ii_+}(t) = \int_0^t G(t-s)\frac{\partial \gamma_{ii_+}}{\partial s}ds \tag{35}$$

with $i = 1 \rightarrow 3$, $i_+ = \mathrm{mod}(i,3)+1$, and $i_- = \mathrm{mod}(i+1,3)+1$.

Application of the recursive formula by Sedef et al. [25] to (34)-(35) yields the stresses at the current time t_{n+1} as follows:

$$\sigma_{ii}^{n+1} = \left[\left(\frac{4}{3}G_\infty + K\right)\varepsilon_{ii}^{n+1} + \left(-\frac{2}{3}G_\infty + K\right)\varepsilon_{i_+ i_+}^{n+1} + \left(-\frac{2}{3}G_\infty + K\right)\varepsilon_{i_- i_-}^{n+1}\right] + \sum_{j=1}^{N_M} H_{j,ii}^{n+1} \tag{36}$$

$$\sigma_{ii_+}^{n+1} = G_\infty \gamma_{ii_+}^{n+1} + \sum_{j=1}^{N_M} H_{j,ii_+}^{n+1} \tag{37}$$

where the functions $H_{j,\alpha\beta}^{n+1}$ $(\alpha,\beta = 1 \rightarrow 3)$ are expressed in an recursive manner as:

$$H_{j,ii}^{n+1} = e^{-\frac{\Delta t^{n+1}}{\tau_j}} H_{j,ii}^n + G_j A_j\left(\frac{4}{3}\Delta\varepsilon_{ii}^{n+1} - \frac{2}{3}\Delta\varepsilon_{i_+ i_+}^{n+1} - \frac{2}{3}\Delta\varepsilon_{i_- i_-}^{n+1}\right) \tag{38}$$

$$H_{j,ii_+}^{n+1} = e^{-\frac{\Delta t^{n+1}}{\tau_j}} H_{j,ii_+}^n + G_j A_j \Delta\gamma_{ii_+}^{n+1} \tag{39}$$

The tri-axial viscoelastic material model described above can be directly applied to 3D continuum elements. In order to apply it to the developed laminated shell elements which ignore the transverse normal stress, a further modification is made by imposing a zero value constraint on the transverse normal stress σ_{33}, leading to the constitutive equations being expressed as follows:

$$\boldsymbol{\sigma}_p^{n+1} = \mathbf{C}_{v,p}^{n+1}\boldsymbol{\varepsilon}_p^{n+1} + \boldsymbol{\sigma}_{\mathrm{hist},p}, \quad \boldsymbol{\sigma}_s^{n+1} = \mathbf{C}_{v,s}^{n+1}\boldsymbol{\varepsilon}_s^{n+1} + \boldsymbol{\sigma}_{\mathrm{hist},s} \tag{40}$$

where $\boldsymbol{\sigma}_p^{n+1} = \left\langle \sigma_{11}^{n+1}, \sigma_{22}^{n+1}, \sigma_{12}^{n+1} \right\rangle^T$ and $\boldsymbol{\sigma}_s^{n+1} = \left\langle \sigma_{13}^{n+1}, \sigma_{23}^{n+1} \right\rangle^T$ denote respectively the planar and transverse shear stresses at time t_{n+1}; $\boldsymbol{\varepsilon}_p^{n+1} = \left\langle \varepsilon_{11}^{n+1}, \varepsilon_{22}^{n+1}, \gamma_{12}^{n+1} \right\rangle^T$ and $\boldsymbol{\varepsilon}_s^{n+1} = \left\langle \gamma_{13}^{n+1}, \gamma_{23}^{n+1} \right\rangle^T$ denote respectively the planar and transverse shear strains at time t_{n+1}; $\mathbf{C}_{v,p}^{n+1}$ and $\mathbf{C}_{v,s}^{n+1}$ are viscoelastic constitutive matrices for respectively the planar and transverse shear stresses/strains at time t_{n+1}; and $\boldsymbol{\sigma}_{hist,p}$ and $\boldsymbol{\sigma}_{hist,s}$ are stresses related to the loading history. The derivations of $\mathbf{C}_{v,p}^{n+1}$, $\mathbf{C}_{v,s}^{n+1}$, $\boldsymbol{\sigma}_{hist,p}$ and $\boldsymbol{\sigma}_{hist,s}$ are provided in Appendix A.

6 APPLICATION TO GLASS STRUCTURES

The laminated shell elements Ln-MITC9 and Ln-MITC6 have been implemented in ADAPTIC [34] v2.14.4. Hereafter, three typical LG problems are modelled with the laminated shell elements, where the benefits of the proposed approach are demonstrated through comparisons with the results of 3D continuum models and monolithic shell models utilising the effective thickness approach outlined in Section 2.

6.1 Laminated glass under biaxial bending

This example relates to a series of biaxial flexural tests conducted by Bennison et al. [31], which were designed to investigate the response of circular LG panels at a wide range of loading rates. The circular LG panel, 100mm in diameter, is composed of two glass bonded by a PVB interlayer. The panel is supported at three points located on a radius $r_2 = 44.7$ mm and is loaded with a circular punch which effectively produces a ring loading with a radius of $r_1 = 4.498$ mm, as depicted in Figure 6. Bennison et al. [31] tested the LG panels with various displacement rates ranging from 10^{-3} to 10^2 mm/s.

From the conducted material tests on the PVB interlayer, Bennison et al. also proposed a generalized Maxwell material model for the description of the shear relaxation modulus [31], which is depicted in Figure 7 corresponding to a reference temperature of 20°C with the material parameters listed for 11 Maxwell components in Table 6. For other temperatures, the time-temperature correspondence principle can be employed, as given in (24)-(25), with coefficients C_1 and C_2 provided as 20.7 and 91.1, respectively.

Herein, due to symmetry, a 60° segment of the circular plate is modelled with meshes of the proposed laminated shell elements. With respect to the fan-shaped geometry, an efficient

mesh type is used, where a ring of the 6-noded triangular element L3-MITC6 is employed surrounding the panel centre and rings of the 9-noded L3-MITC9 element are employed for the remaining part. A 10×10 mesh, denoted as L3-MITC6|9, as shown in Figure 8, provides a convergent solution, which is thus used to reproduce some of the tests and compare with both the experimental results and the numerical predictions of 3D continuum models consisting of four layers of elements for each glass ply and two layers for the PVB interlayer [31].

Bennison et al. used uniaxial electrical-resistance strain gauges to record the strain of the lower ply on the supported (lower) glass surface along with the applied force for one LG test, where the punch force was applied with a displacement rate of 10^{-3}mm/s at a constant temperature of 22.8°C [31]. Figure 9 records the principal stress at the bottom surface of the lower glass ply against the applied punch force for the 10×10 laminated shell model. Also provided are the experimental results and the numerical predictions of the 3D continuum model. Clearly, the results of the laminated shell model are in excellent agreement with the experimental results and the numerical predictions of the more computationally demanding 3D model.

The through-thickness distribution of the principal stress at the panel centre is investigated for a given central deflection of δ = 0.6mm. Two normalised displacement loading rates have been considered: $v^* =0.675$ and $6.75×10^8$, with the normalised loading rate defined by Bennison et al. [31] as follows:

$$v^* = \frac{va_T\tau^*}{\delta}$$

where v is the real displacement loading rate (mm/s), δ = 0.6mm is the central deflection, τ^* denotes the characteristic time for G(t) to relax to a value of around 1MPa, which is given as 1127s, and a_T is a coefficient associated with temperature, as defined in (25).

Figure 10 shows that the predicted stress distribution of the L3-MITC6|9 shell model matches well with the 3D continuum model by Bennison et al. [31] at both loading rates.

The variation of the stress distribution with the loading rate, corresponding to a 0.6mm maximum deflection, is investigated. Define the normalised stresses at the positions 'i' and 'o', shown in Figure 6, as follows:

$$\zeta^i = \frac{\sigma_1^i}{\sigma_1^m}, \quad \zeta^o = \frac{\sigma_1^o}{\sigma_1^m}$$

where σ_1^i and σ_1^o are the maximum principal stresses at the bottom of the upper and the lower glass ply, respectively, corresponding to a central deflection of $\delta = 0.6$mm, and σ_1^m is the maximum principal stress for a monolithic glass pane of thickness $2h_g$ with the same punch force. The normalised stress-loading rate curves predicted by the L3-MITC6|9 laminated shell model are depicted in Figure 11. At a relatively slow loading rate, the PVB interlayer has a limited shear stiffness to transfer shear forces, resulting in rapid development of stresses in each glass ply. For a rapid loading rate, on the other hand, the PVB interlayer exhibits stiff material properties, which leads to the three layers working as a whole and hence reducing the normalised stress at position 'o' to around 1.0 and position 'i' to an even smaller value. As can be observed from the figure, the results of the laminated shell model are in good agreement with the curves obtained by the 3D continuum model [31], which verifies the accuracy of the L3-MITC6|9 shell model and the viscoelastic material model in the simulation of LG. Also shown in Figure 11 are the results of the FSDT-based shell model with the same 10×10 mesh, which are obtained by restraining all additional zigzag parameters in the laminated shell model. The deviation of the FSDT results from the others indicates the significant zigzag effects of the LG panels throughout the considered range of loading rates due to the modulus mismatch between glass and PVB. On the other hand, as indicated in the figure, this deviation of results reduces with much higher loading rates.

6.2 Buckling analysis of laminated glass fin

In recent years, not only has LG been widely used for secondary structural components (such as curtain wall glazing), but it has also become increasingly adopted for structural applications (Figure 12.a). LG members that are used in real structures are typically associated with large slenderness, thus posting equal importance of stability analysis to cross-sectional strength analysis. Figure 12.b depicts a partial LG sub-structure extracted from the glass structure shown in Figure 12.a, where two halves of curtain wall glazing panels are supported by a LG fin with the employment of the adhesive silicone bond between the fin and

the glazing panes, which provides a continuous elastic support along the vertical glazing edge, with a plan view as depicted in Figure 13. A uniform transverse loading is applied to the two halves of glazing to represent the wind load. For design purpose, ASTM E1300-12a [4] suggests using a linear elastic material model for the PVB with the shear relaxation modulus for a 3s load duration at a 50°C operation temperature for the analysis of wind load. Therefore, a linear elastic material model is used, where the bulk modulus is 2.0GPa and the shear modulus is 0.44MPa, which is extracted from the shear relaxation model proposed by Bennison et al. [31] (Table 6) for a load duration of 3s at a 50°C operation temperature. The geometric, material and loading conditions are listed in Table 7. A static analysis is performed to determine the stability of this partial structure under the wind load.

The continuous elastic support provided by the silicone joint is modelled with matrix elements along the edge. Since silicone is associated with a large Poisson's ratio (ν=0.499), the silicone joint undergoes relatively small bulk deformations under loading. In order to obtain the effective stiffness components of the matrix elements, a 3D continuum model with a fine mesh of a 20-noded brick element [35] is employed to model the silicone joint, which has a width $t_g = 36$mm, a depth $t_s = 20$mm, and a height $H = 50$mm. As shown in Figure 14, the top and bottom surfaces are restrained in the y direction, whereas the left surface (at $x = 0$) is fully restrained. Three displacement modes are applied on the right surface (at $x = t_s$), respectively:

(1) elongation in the x direction, at $x = t_s$: $u_x = 10^{-6}$ m, $u_y = u_z = 0$;

(2) shearing in the z direction, at $x = t_s$: $u_z = 10^{-6}$ m, $u_x = u_y = 0$;

(3) rotation about the y axis, at $x = t_s$: $u_x = 10^{-6}(z - t_g/2)$ m, $u_y = 0$.

The three models then correspond to respectively a tensile force F_x, a shear force F_z, and a bending moment M_{ry}, respectively, which result in the effective stiffness terms as follows:

$$k_x = \frac{F_x}{u_x H} = 6.32 \times 10^6 \, \text{N}/\text{m}^2, \, k_z = \frac{F_z}{u_z H} = 6.28 \times 10^5 \, \text{N}/\text{m}^2, \, k_{ry} = \frac{M_{ry}}{r_y H} = 405.6 (\text{N} \cdot \text{m})/\text{m}.$$

Figure 15 depicts the deformation modes of the silicone joint cross-section for a uniform elongation and a uniform rotation, respectively, which clearly demonstrates the influence of small bulk deformations on the overall mode. In the following analyses, the effective stiffness

terms, along with the element size along the y direction, are used for the spring matrix elements.

The partial fin-glazing structure is simulated with a laminated shell element model, where the three-play glass fin is modelled with a 16×4 mesh of the L5-MITC9 element, and each of the half two-play glazing panels is modelled with a 16×8 mesh of the L3-MITC9 element. The boundary conditions of the partial model are depicted in Figure 16.a. The structure is more vulnerable to the suction load, hence uniform loads in the negative x direction are considered in this buckling analysis. Besides the fin-glazing model, a more simplified fin model is also used which consists of the glass fin only with the same element size. Figure 16.b shows the boundary conditions of the simplified model, and the suction load is assumed to be a uniform line load applied to the silicone joint. Both considered models provide convergent solutions. Figure 17 depicts the equilibrium paths of the z displacement at Point A with both the fin-glazing model and the fin model. Note that for the fin-glazing model the effective suction load is obtained by dividing the sum of the uniform loading on the glazing panels, subtracting the reaction forces in x direction at the top and bottom glazing edges (illustrated in Figure 16.a), by the glazing width. It is evident that the predicted buckling curve of the fin model matches well that of the fin-glazing model, which is hereafter used to assess the accuracy and efficiency of various FE modelling methods.

For the fin model, the equilibrium path of the z displacement at Point A is predicted with four FE models. Model 1 corresponds to the 16×4 laminated shell model with the employment of the L5-MITC9 element. By restraining the entire additional zigzag DOFs, an FSDT-based laminated shell model is also obtained for comparison, which is denoted as Model 2. A 16×4 mesh of the 9-noded monolithic MITC9 element, denoted as Model 3, is also considered, where an effective thickness of 17.68 mm in accordance with Section 2.2 is employed as the monolithic glass thickness. Apart from the laminated and monolithic shell element models, the buckling analysis is also performed with a 3D continuum model using 20-noded brick elements, where the fin is discretised into 4 elements along the x-axis and 50 elements along the y-axis, and each layer is discretised into 2 elements through the thickness. The solid model, denoted as Model 4, provides a reference solution for comparison.

The load-displacement curves of various models are depicted in Figure 18, with the predicted buckling load and the number of DOFs used for each model listed in Table 8. Clearly, Model 2 employing FSDT corresponds to a much stiffer response than the others owing to the assumption of a linear displacement variation through the thickness, which indicates a significant zigzag effect that cannot be ignored. Although the monolithic shell model (Model 3) takes into account the material mismatch by employing a reduced effective thickness, the model underestimates the buckling load, which may lead to an over-conservative design. It is also observed that L3-MITC9 model (Model 1) shows comparable accuracy with the solid model but is 71.4 times faster, as also confirmed by comparing the total number of DOFs for the various models in Table 8. Figure 19 also depicts the through-thickness distribution of the stress component σ_y at point A for Models 1 and 4, which again confirms the accuracy of the proposed approach based on laminated shell elements.

The influence of the interlayer material stiffness on the predictions of the equilibrium paths is investigated in Figure 20, where four different shear modulus values for PVB are considered (0.44 MPa, 4.4 MPa, 44 MPa, and 440MPa) while the bulk modulus remains constant at 2.0 GPa. For the considered shear modulus values of the PVB, the corresponding effective thicknesses of the monolithic glass are 17.68 mm, 20.38mm, 30.06mm and 37.35mm, respectively. The buckling curves of monolithic shell models employing the MITC9 element with various PVB shear modulus values are compared against the results by the laminated shell models employing the L5-MITC9 element, as depicted in Figure 20. These results indicate that the monolithic shell model based on an effective thickness underestimates the buckling load for a small-to-moderate PVB shear modulus. For the largest PVB shear modulus of 440MPa, both models yield identical equilibrium paths, where the shear stiffness of the PVB interlayer is sufficient to transmit shear forces.

The accuracy of the effective thickness method for a 2-ply LG fin (2×12mm glass +1×1.52mm PVB) with the same planar dimensions is also investigated. Here again, the laminated shell model corresponds to a 16×4 mesh of the L3-MITC9 elements, and the monolithic shell model corresponds to a 16×4 mesh of the MITC9 element with the effective thickness calculated with reference to the ASTM E1300-12a [4]. For the considered shear

modulus values of PVB (0.44 MPa, 4.4 MPa, 44 MPa, and 440MPa), the corresponding effective thicknesses of the monolithic glass are 15.33 mm, 16.88mm, 21.89mm and 24.97mm, respectively. The resulting equilibrium paths with various interlayer shear stiffness values and models are depicted in Figure 21, which shows the same trend as for the three-ply LG fin.

6.3 Creep of laminated glass stair

Owing to the viscoelastic mechanical behaviour of the PVB interlayer, LG is associated with noticeable creep under long-duration loading. Here, the creep behaviour of a typical LG stair is considered, as shown in Figure 22. The LG stair, which is 1.8m wide and 0.3m deep, is installed horizontally with both edges simply supported. The glass stair is composed of four 12mm glass plies and three 1.52mm PVB interlayers. The material parameters of glass are $E = 70\text{GPa}$ and $\nu = 0.2$. The linear viscoelastic model proposed by Bennison et al. [31] is used for the PVB, where the parameters of the shear relaxation are listed in Table 6 and the bulk modulus is fixed at $K = 2.0\text{GPa}$. With the use of the viscoelastic material model for PVB, the creep behaviour of the glass stair under a self-weight of $w = 1219.7 \text{ N/m}^2$ with time at different operation temperatures can be analysed.

Considering the constant loads and the long time span of the analysis, this problem can be regarded as a pseudo static problem. A static analysis is performed on a quarter model of the stair, which uses an 8×2 mesh of the L7-MITC9 elements to provide a convergent solution. In the following, the influence of loading duration and operation temperature is investigated and the results are discussed.

Figure 23 depicts the time-history curves of the central deflection with various operation temperatures for 10 years, which shows that for an operation temperature of 30°C the stair deflection approaches to the asymptotic value (3.05mm) at around 98 days after installation, whereas for an operation temperature of 10°C the deflection at 10 years is 1.92mm, which is much lower than for the other considered temperatures. The maximum 10-year deflections for different operation temperatures have also been predicted by monolithic shell models with effective thicknesses, which employ the same mesh but with the MITC9 element utilising an

effective thickness. For the considered operation temperatures (10°C, 20°C, 24°C, 30°C), the 10-year shear modulus values of PVB are extracted from the generalised Maxwell model with the material properties given in Table 6. Accordingly, the shear modulus values corresponding to 10°C, 20°C, 24°C, and 30°C operation temperatures are determined as 383.12kPa, 51.86 kPa, 51.72 kPa, and 51.72 kPa, respectively. The employment of the incremental effective thickness approach then results in effective thicknesses of 19.30 mm, 19.08 mm, 19.08 mm, and 19.08 mm, respectively for the considered cases. Table 9 lists the predicted maximum 10-year deflections by monolithic shell models with an 8×2 mesh of the MITC9 element, which are compared against the reference values by the laminated shell models. Clearly, the effective thickness approach obtains very conservative predictions of the maximum deflection despite the fact that the stair is simply supported along two edges only and a uniform loading is applied.

Assume that during operation an additional patch load p=2000N/m² is exerted at some point in time on the glass stair, which stays permanent afterwards, as shown in Figure 24. Three loading histories are considered, as shown in Figure 25. The deflection time histories at a 20°C operation temperature with various load histories are depicted in Figure 26, where it is evident that the deflections converge to around 4.4 mm after a sufficiently long duration. Results with various operation temperatures for load history 1 are also shown in Figure 27. Clearly, temperature has a major influence on the time required for the deflections to reach the maximum steady state value.

7   CONCLUSIONS

This paper presents a multi-layer shell modelling approach for the analysis of multi-ply LG structures, where 6-noded and 9-noded laminated shell elements specific to laminations with an alternating stiff/soft lay-up are employed, and viscoelastic material properties of PVB are considered.

LG structures have been widely employed in structural engineering, which is characterised by a significantly large stiffness mismatch through the LG thickness and the variation of PVB mechanical behaviour with loading duration and temperature. The effective thickness

approach is widely adopted in the current LG design standards owing to the simplicity in LG design. However, the effective thickness method is based on a restrictive set of assumptions which typically render in accurate for general geometric configurations of plates and shells, and its generalisation to multi-ply LG applications is subject to further ambiguity and associated inaccuracy.

Two laminated shell elements, Ln-MITC6 and Ln-MITC9, have been developed, which are based on a lamination model that captures the distinctive characteristics of the through-thickness distribution of planar displacements and transverse shear strains for LG. The underlying kinematic assumptions lead to a minimal number of zigzag displacement parameters and a decoupled relationship between layers by not imposing inter-laminar continuity constraints of transverse shear stresses. The accuracy of the lamination model is illustrated in this paper with a 1D LG beam problem, where the results match well with the solution by a 2D plane stress analysis. In order to consider the influence of temperature and loading rates to the behaviour of LG members, a viscoelastic material model is adapted and incorporated in the developed laminated shell elements for modelling the PVB interlayer.

Several LG problems are finally analysed with laminated shell models, considering typical two-ply and multi-ply problems relating to deflection, stability and creep analysis. The accuracy and efficiency of the proposed approach are compared with the effective thickness method and 3D continuum models. It is concluded that the proposed approach based on the laminated shell Ln-MITC6 and Ln-MITC9 elements provides comparable accuracy with 3D continuum models at a much reduced computation time, and that the effective thickness method can be subject to gross inaccuracy that typically renders too conservative for application in design practice.

REFERENCES

[1] Bennison SJ, Qin MHX, Davies PS. High-performance laminated glass for structurally efficient glazing. *Innovative Light-Weight Structures and Sustainable Facades*, 2008: 1-12.

[2] Shitanoki Y, Bennison SJ, Koike Y. Structural behavior thin glass ionomer laminates with optimized specific strength and stiffness. *Composite Structures* 2015; **125**: 615-620.

[3] Lenk P, Lancaster F. Stability analysis of structural glass systems. In: *Challenging Glass 3: Conference on Architectural and Structural Applications of Glass*. IOS Press: 2012; 475.

[4] American Society Testing Materials. E1300-12a. Standard Practice for Determining Load Resistance of Glass in Buildings. ASTM International, 2012.

[5] CEN-TC129WG8. prEN 13474: Glass in Building – Determination of the Strength of Glass Panes by Calculation and Testing. Project of European Standard under Enquiry, 2012.

[6] Galuppi L, Royer-Carfagni GF. Effective thickness of laminated glass beams: new expression via a variational approach. *Engineering Structures* 2012; **38**: 53-67.

[7] Galuppi L, Royer-Carfagni GF. Enhanced Effective Thickness of multi-layered laminated glass. *Composites Part B: Engineering* 2014; **64**: 202-213.

[8] Reddy JN. On refined computational models of composite laminates. *International Journal for Numerical Methods in Engineering* 1989; **27**(2):362-382.

[9] Robbins DH, Reddy JN. Modelling of thick composites using a layerwise laminate theory. *International Journal for Numerical Methods in Engineering* 1993; **36**(4): 655-677.

[10] Reddy JN. Mechanics of laminated composite plates and shells: Theory and analysis. CRC press; 2003.

[11] Murakami H. Laminated composite plate theory with improved in-plane responses. *Journal of Applied Mechanics* 1986; **53**(3): 661-666.

[12] Carrera E. C0 Reissner-Mindlin multilayered plate elements including Zigzag and Interlaminar stress continuity. *International Journal for Numerical Methods in Engineering* 1996;**39**(11):1797-1820.

[13] Carrera E. Evaluation of layerwise mixed theories for laminated plates analysis. *AIAA Journal* 1998; **36**(5): 830-839.

[14] Carrera E. An assessment of mixed and classical theories on global and local response of multilayered orthotropic plates. *Composite Structures* 2000; **50**(2): 183-198.

[15] Carrera E. Historical review of zig-zag theories for multilayered plates and shells. *Applied Mechanics Reviews* 2003; **56**(3): 287-308.

[16] Carrera E. On the use of the Murakami's zig-zag function in the modeling of layered plates and shells. *Computers & Structures* 2004; **82**(7): 541-554.

[17] Bati SB, Ranocchiai G, Reale C, et al. Time-dependent behavior of laminated glass. *Journal of Materials in Civil Engineering* 2009; **22**(4): 389-396.

[18] Liang Y, Izzuddin B A. Nonlinear analysis of laminated shells with alternating stiff/soft lay-up. *Composite Structures* 2015; **133**: 1220-1236.

[19] Liang Y. Nonlinear analysis of composite shells with application to glass structures, PhD Thesis, Imperial College London, 2015.

[20] Kim D, Bathe K. A triangular six-node shell element. *Computers & Structures* 2009; **87**(23), 1451-1460.

[21] Bathe KJ, Lee PS, Hiller JF. Towards improving the MITC9 shell element. *Computers & Structures* 2003; **81**(8):477-489.

[22] Wisniewski K, Panasz P. Two improvements in formulation of nine-node element MITC9. *International Journal for Numerical Methods in Engineering* 2013; **93**(6):612-634.

[23] Izzuddin BA. An enhanced co-rotational approach for large displacement analysis of plates. *International Journal for Numerical Methods in Engineering* 2005;**64**(10):1350-1374.

[24] Izzuddin BA, Liang Y. Bisector and zero-macrospin co-rotational systems for shell elements. *International Journal for Numerical Methods in Engineering* 2016; **105**(4): 286-320.

[25] Sedef M, Samur E, Basdogan C. Real-time finite-element simulation of linear viscoelastic tissue behavior based on experimental data. *Computer Graphics and Applications, IEEE* 2006; **26**(6): 58-68.

[26] Wölfel E. Nachgiebiger verbund – eine näherungslösung und deren anwendungsmöglichkeiten. Stahlbau 1987;6:173-80.

[27] Bennison SJ, Stelzer I. Structural properties of laminated glass. In: *Short course, glass performance days*. Tampere, Finland. 2009.

[28] Calderone I, Davies PS, Bennison SJ, Xiaokun H, Gang L. Effective laminate thickness for the design of laminated glass. In: *Proceedings of Glass performance days*. Tampere, Finland. 2009.

[29] Zenkert D. *The Handbook of Sandwich Construction*. EMAS; 1997.

[30] Liang Y, Izzuddin BA. Large displacement analysis of sandwich plates and shells with symmetric/asymmetric lamination. *Computers & Structures* 2016; **166**: 11-32.

[31] Bennison S, Jagota A, Smith C. Fracture of glass/poly (vinyl butyral)(Butacite®) laminates in biaxial flexure. *Journal of the American Ceramic Society* 1999; **82**(7): 1761-1770.

[32] Shaw M, MacKnight W. *Introduction to polymer viscoelasticity*. John Wiley & Sons; 2005.

[33] Ferry J. *Viscoelastic properties of polymers*. John Wiley & Sons; 1980.

[34] Izzuddin BA. Nonlinear dynamic analysis of framed structures. PhD Thesis, Department of Civil Engineering, Imperial College, University of London, 1991.

[35] Zeinkiewicz OC, Taylor RL, Zhu JZ. *The finite element method: its basis and fundamentals*. 2005.

Appendix A: Linear viscoelastic model for 2D shell elements

In order to apply the viscoelastic material model described in Section 5.2 to 2D elements, the zero value constraint on the transverse normal stress σ_{33} needs to be imposed, which yields a transverse normal strain ε_{33}^{n+1} expressed as:

$$\varepsilon_{33}^{n+1} = \frac{\hat{b}}{\hat{a}}\left(\varepsilon_{11}^{n+1} + \varepsilon_{22}^{n+1}\right) - \frac{\hat{c}}{\hat{a}} \tag{A1}$$

in which:

$$\hat{a} = \frac{4}{3}G_{\infty} + K + \frac{4}{3}\sum_{j=1}^{N_M} G_j A_j, \quad \hat{b} = \frac{2}{3}G_{\infty} - K + \frac{2}{3}\sum_{j=1}^{N_M} G_j A_j \tag{A2}$$

$$\hat{c} = \sum_{j=1}^{N_M} G_j A_j \left[\frac{2}{3}\left(\varepsilon_{11}^n + \varepsilon_{22}^n\right) - \frac{4}{3}\varepsilon_{33}^n\right] + \sum_{j=1}^{N_M} e^{-\frac{\Delta t}{\tau_j}} H_{j,33}^n \tag{A3}$$

By substituting (A1) into (36)-(37), (40) is obtained with the matrices $\mathbf{C}_{v,p}^{n+1}$ and $\mathbf{C}_{v,s}^{n+1}$ expressed as:

$$\mathbf{C}_{v,p}^{n+1} = \begin{bmatrix} \dfrac{(\hat{a}+\hat{b})(\hat{a}-\hat{b})}{\hat{a}} & -\dfrac{\hat{b}(\hat{a}+\hat{b})}{\hat{a}} & 0 \\ -\dfrac{\hat{b}(\hat{a}+\hat{b})}{\hat{a}} & \dfrac{(\hat{a}+\hat{b})(\hat{a}-\hat{b})}{\hat{a}} & 0 \\ 0 & 0 & \hat{d} \end{bmatrix}, \quad \mathbf{C}_{v,s}^{n+1} = \begin{bmatrix} \hat{d} & 0 \\ 0 & \hat{d} \end{bmatrix} \tag{A4}$$

with:

$$\hat{d} = G_{\infty} + \sum_{j=1}^{N_M} G_j A_j \tag{A5}$$

where A_j is given in (33).

The stress vectors $\boldsymbol{\sigma}_{\text{hist},p}$ and $\boldsymbol{\sigma}_{\text{hist},s}$ are then derived as:

$$\boldsymbol{\sigma}_{\text{hist},p} = \frac{\hat{b}\hat{c}}{\hat{a}}\begin{Bmatrix} 1 \\ 1 \\ 0 \end{Bmatrix} - \sum_{j=1}^{N_M} G_j A_j \left[\begin{array}{ccc|c} \frac{4}{3} & -\frac{2}{3} & -\frac{2}{3} & 0 \\ \hline -\frac{2}{3} & \frac{4}{3} & -\frac{2}{3} & 0 \\ \hline 0 & 0 & 0 & 1 \end{array}\right] \begin{Bmatrix} \varepsilon_{11}^n \\ \varepsilon_{22}^n \\ \varepsilon_{33}^n \\ \gamma_{12}^n \end{Bmatrix} + \sum_{j=1}^{N_M} e^{-\frac{\Delta t}{\tau_j}}\begin{Bmatrix} H_{j,11}^n \\ H_{j,22}^n \\ H_{j,12}^n \end{Bmatrix} \tag{A6}$$

$$\boldsymbol{\sigma}_{\text{hist,s}} = -\sum_{j=1}^{N_M} G_j A_j \begin{Bmatrix} \gamma_{13}^n \\ \gamma_{23}^n \end{Bmatrix} + \sum_{j=1}^{N_M} e^{-\frac{\Delta t}{\tau_j}} \begin{Bmatrix} H_{j,13}^n \\ H_{j,23}^n \end{Bmatrix} \tag{A7}$$

Table 1: Geometric, material, loading, and boundary conditions of the simply-supported LG beam.

Geometric parameters	Two-ply LG: lay-up: 2×12mm glass + 1×1.52mm PVB; thickness h=25.52mm Four-ply LG: lay-up: 4×12mm glass + 3×1.52mm PVB; thickness h=52.56mm Beam length: L=10h
Material parameters	Glass: Young's modulus E=70.0 GPa, Poisson's ratio ν=0.2 PVB (short duration): shear modulus G=100MPa, bulk modulus K=2.0GPa PVB (long duration): shear modulus G=1.0 MPa, bulk modulus K=2.0GPa
Loading condition	Transverse concentrated force: P=100N/m
Boundary conditions	$u_{z0}(0) = u_{z0}(L) = 0$ $u_{x0}(L/2)=0$

Table 2: Rotation of the normal for each layer at the quarter span (x=L/4) by 2D analysis.

Layer	Rotation of layer normal at quarter span (rad)			
	Case 1	Case 2	Case 3	Case 4
1	1.46E-05	5.29E-06	2.59E-05	2.86E-06
2	-1.14E-04	-1.87E-05	-2.00E-04	-7.63E-06
3	1.46E-05	5.29E-06	2.59E-05	2.84E-06
4	-	-	-2.04E-04	-1.06E-05
5	-	-	2.59E-05	2.84E-06
6	-	-	-2.00E-04	-7.63E-06
7	-	-	2.59E-05	2.86E-06

Table 3: Percentage contribution of each layer to the transverse shear strain energy at the quarter span (x=L/4) by 2D analysis.

| Layer | Relative percentage of transverse shear strain energy | | | |
	Case 1	Case 2	Case 3	Case 4
1	7.53%	2.31%	0.20%	0.40%
2	84.94%	95.38%	32.59%	26.69%
3	7.53%	2.31%	0.24%	1.21%
4	-	-	33.94%	43.40%
5	-	-	0.24%	1.21%
6	-	-	32.59%	26.69%
7	-	-	0.20%	0.40%

Table 4: Rotation of the normal for each layer at the quarter span (x=L/4) by the lamination model.

Layer	Rotation of layer normal at quarter span (rad)			
	Case 1	Case 2	Case 3	Case 4
1	1.46E-05	5.28E-06	2.59E-05	2.85E-06
2	-1.14E-04	-1.87E-05	-2.00E-04	-7.63E-06
3	1.46E-05	5.28E-06	2.59E-05	2.85E-06
4	-	-	-2.04E-04	-1.06E-05
5	-	-	2.59E-05	2.85E-06
6	-	-	-2.00E-04	-7.63E-06
7	-	-	2.59E-05	2.85E-06

Table 5: Percentage contribution of each layer to the transverse shear strain energy at the quarter span (x=L/4) by the lamination model.

Layer	Relative percentage of transverse shear strain energy			
	Case 1	Case 2	Case 3	Case 4
1	8.30%	2.64%	0.19%	0.67%
2	83.40%	94.72%	32.59%	26.68%
3	8.30%	2.64%	0.25%	0.90%
4	-	-	33.94%	43.48%
5	-	-	0.25%	0.90%
6	-	-	32.59%	26.68%
7	-	-	0.19%	0.67%

Table 6: Terms of the generalised Maxwell series description [31].

j	G_j/G_0	τ_j(s)
1	0.1606000	3.2557E-11
2	0.0787770	4.9491E-09
3	0.2912000	7.2427E-08
4	0.0711550	9.8635E-06
5	0.2688000	2.8059E-03
6	0.0895860	1.6441E-01
7	0.0301830	2.2648E+00
8	0.0076056	3.5364E+01
9	0.0009634	9.3675E+03
10	0.0004059	6.4141E+05
11	0.0006143	4.1347E+07

Instantaneous shear modulus $G_0 = 0.471$GPa; WLF parameters $C_1 = 20.7$ and $C_2 = 91.1$, at a reference temperature of 20°C.

Table 7: Geometric, material and loading parameters for the LG buckling problem.

Geometric parameters	LG fin:
	    lay-up: 3×12mm glass + 2×1.52mm PVB
	    height: H = 10m
	    depth: D = 0.4m
	 LG glazing:
	    lay-up:2×10mm glass + 1×1.52mm PVB
	    height: H = 10m
	    half-width: W = 1m
	 Silicone joint:
	    height: H = 10m
	    width (in z direction): t_g = 36mm
	    depth (in x direction): t_s = 20mm

Material parameters	Glass: Young's modulus E=70.0 GPa, Poisson's ratio ν=0.2 PVB3s@50°C: shear modulus G=0.44MPa, bulk modulus K=2.0GPa Silicone: Young's modulus E=1.4MPa, Poisson's ratio ν=0.499
Loading parameter	Uniform suction load on glazing

Table 8: Accuracy and efficiency comparisons of results using different models.

Model	Critical suction load (kN/m)	Number of DOFs
1	4.47	2660
2	-	1510
3	3.67	1510
4	4.48	30747

Table 9: The accuracy of predicted 10-year deflections by effective thickness approach with various operation temperatures.

Operation temperature	10-year deflection (mm)	
	L7-MITC9	MITC9
10°C	1.92	3.59 (+87.0%)
20°C	3.05	3.68 (+20.7%)
24°C	3.05	3.68 (+20.7%)
30°C	3.05	3.68 (+20.7%)
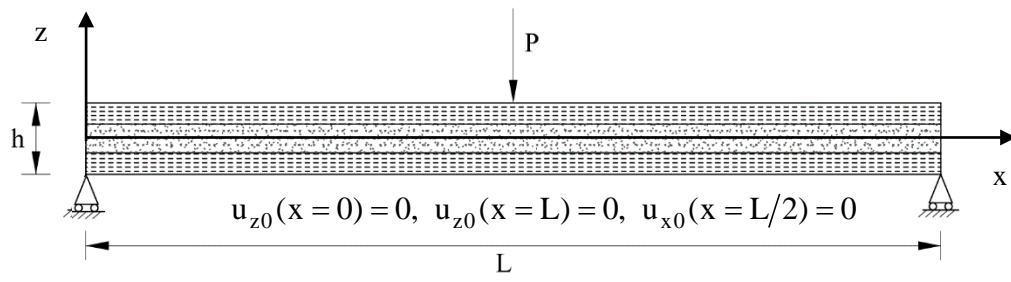
Figure 1: A simply-supported LG beam loaded with a transverse force at the midspan.
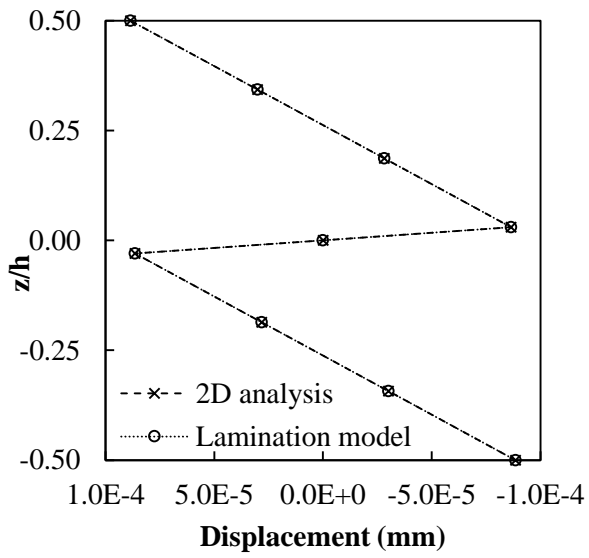
a. Case 1
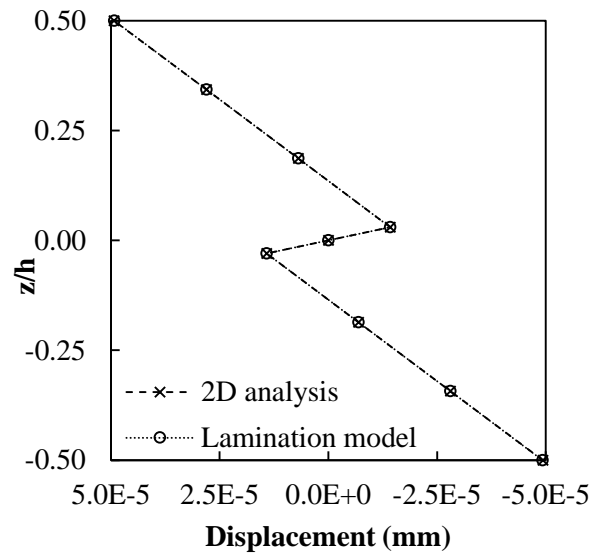
b. Case 2
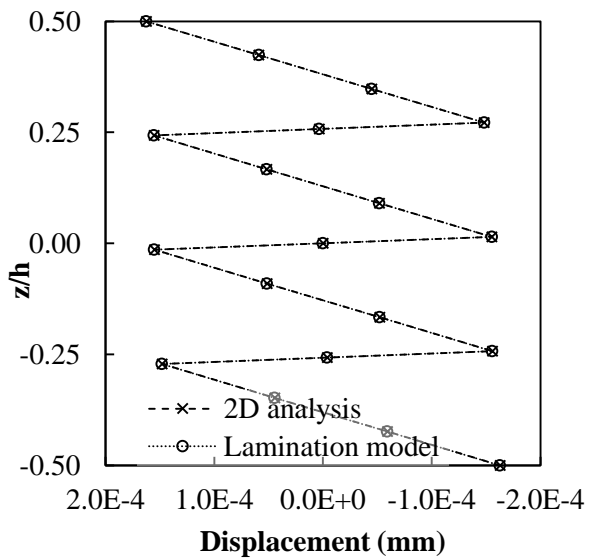
c. Case 3
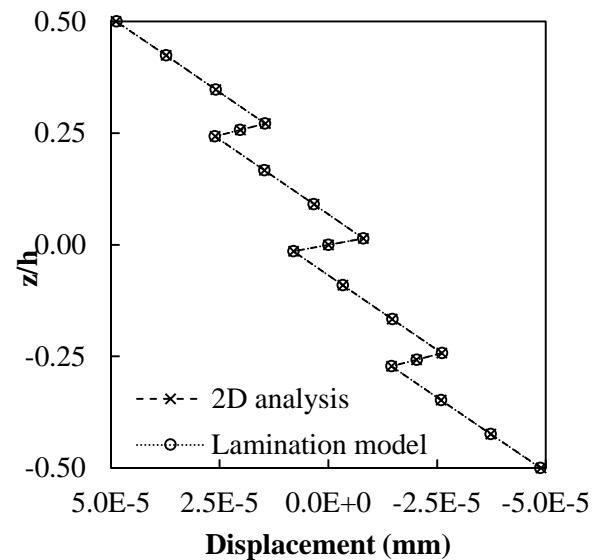
d. Case 4

Figure 2: Through-thickness distributions of the longitudinal displacement at the quarter-span for the considered cases.
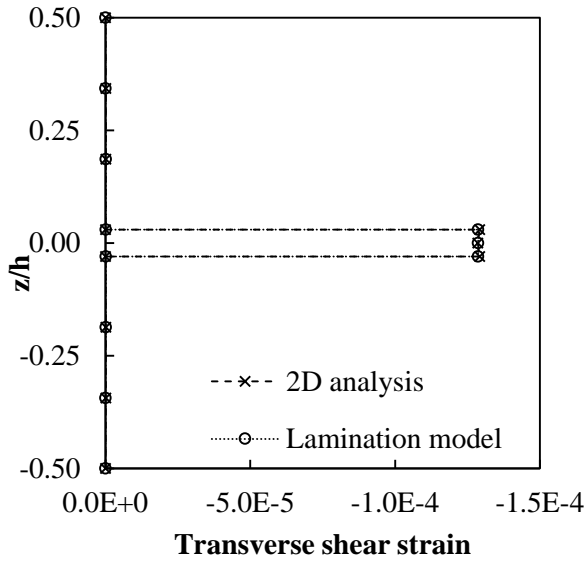
a. Case 1
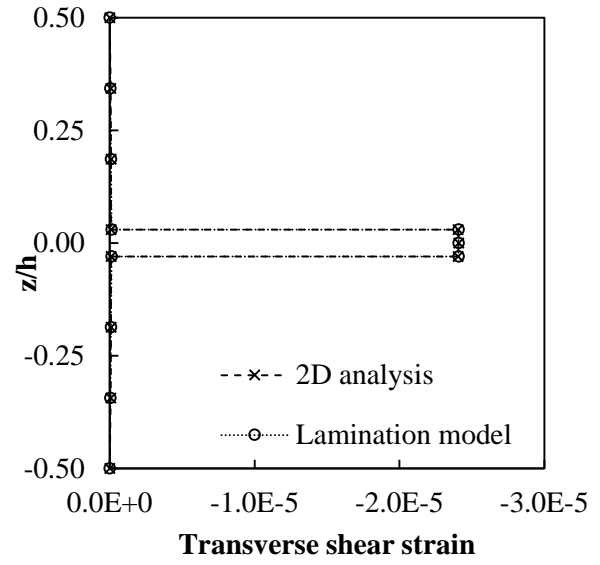
b. Case 2
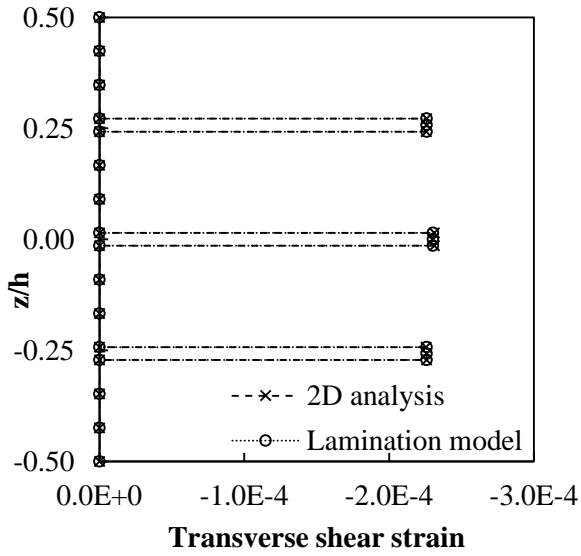
c. Case 3
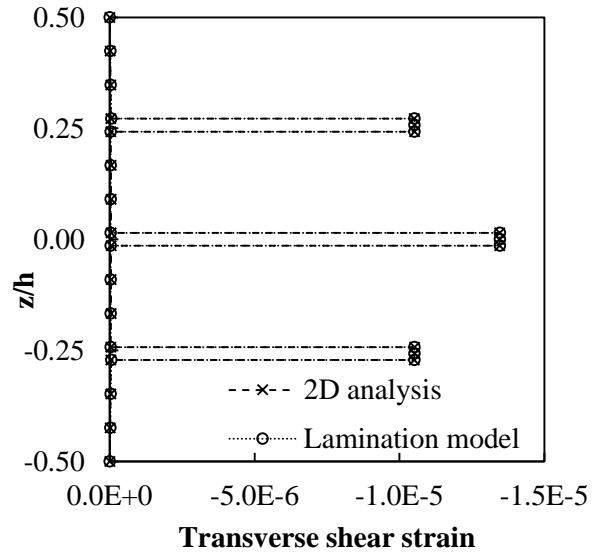
d. Case 4

Figure 3: Through-thickness distributions of transverse shear strain at the quarter-span for the considered cases.
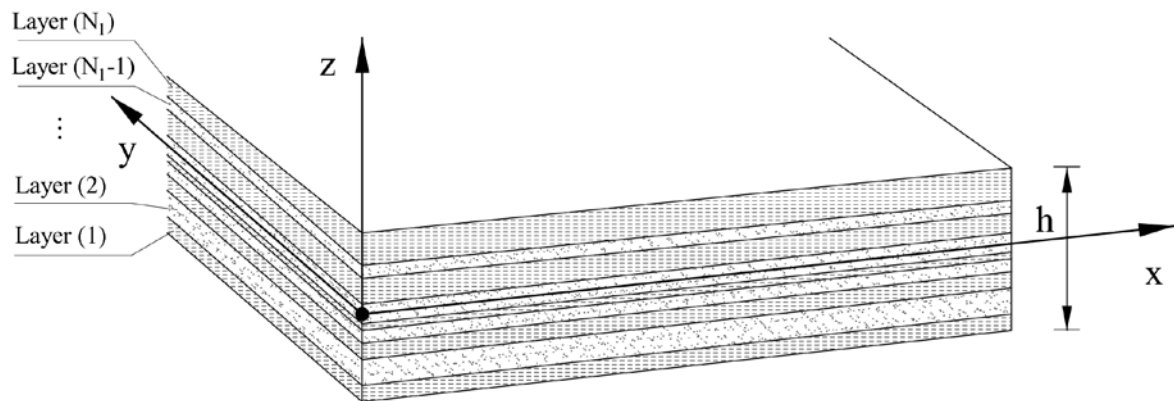
Figure 4: Local coordinate system and layer numbering for LG panel.
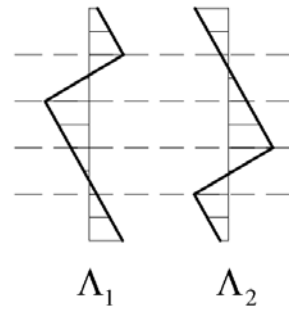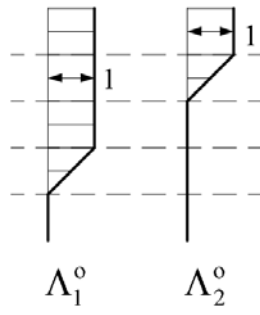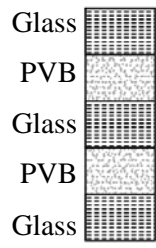
a. Lay-up	b. Λ_j^o before orthogonalisation	c. Λ_j after orthogonalisation

Figure 5: Zigzag modes for a three-ply LG lay-up.
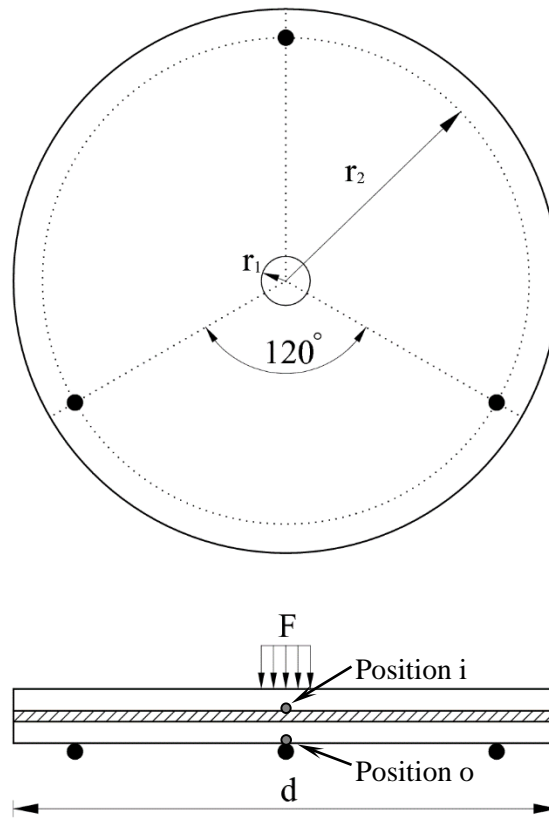
Figure 6: Schematic drawing of the biaxial bending tests on LG panels [31].
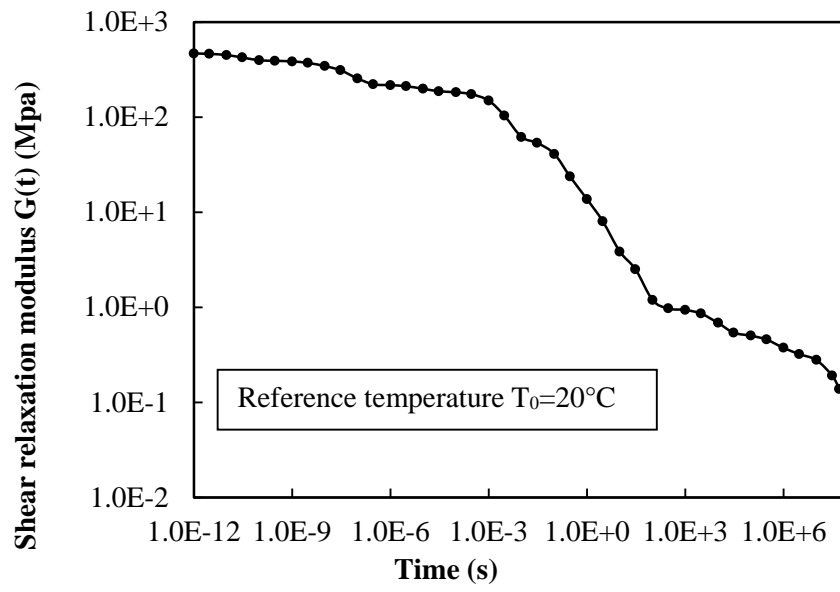
Figure 7: Plot of shear relaxation data for PVB at a reference temperature of 20°C [31].
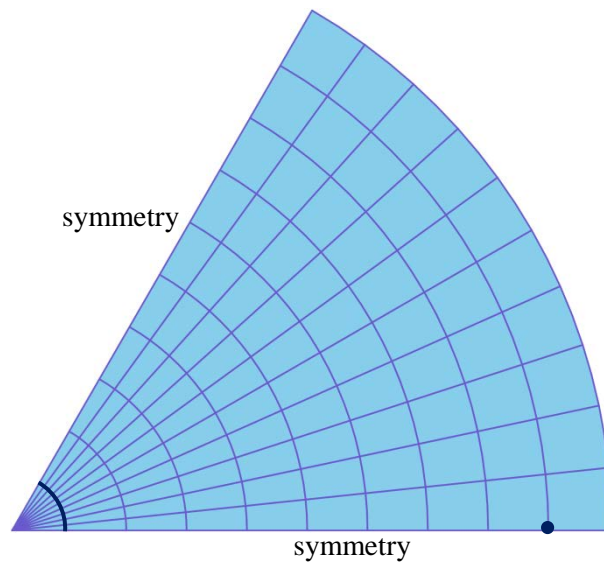
Figure 8: A sixth model of the LG problem (bold line denotes ring loading; point denotes support).
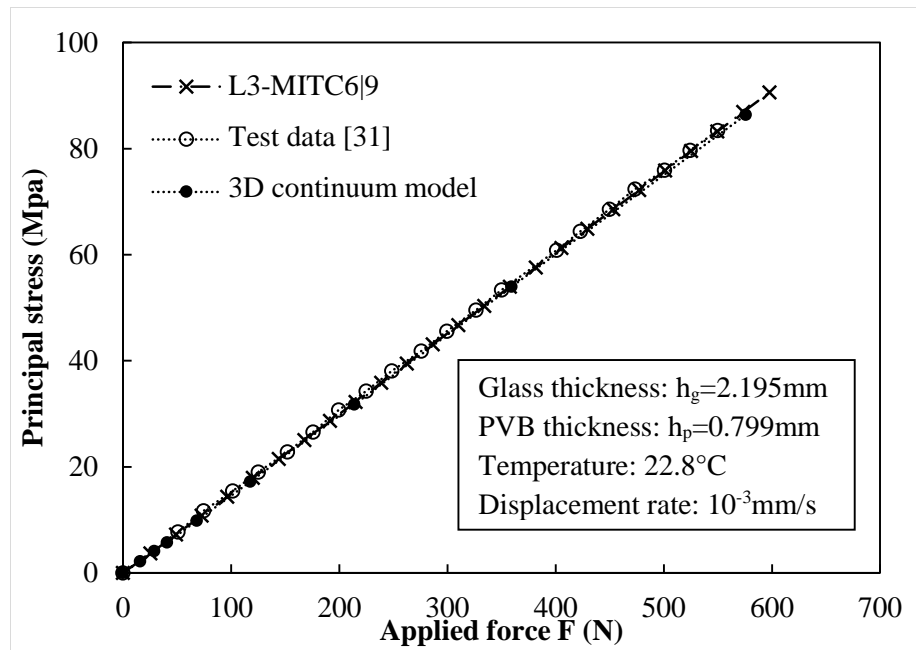
Figure 9: The principal stress-force curves of experimental data and numerical models.
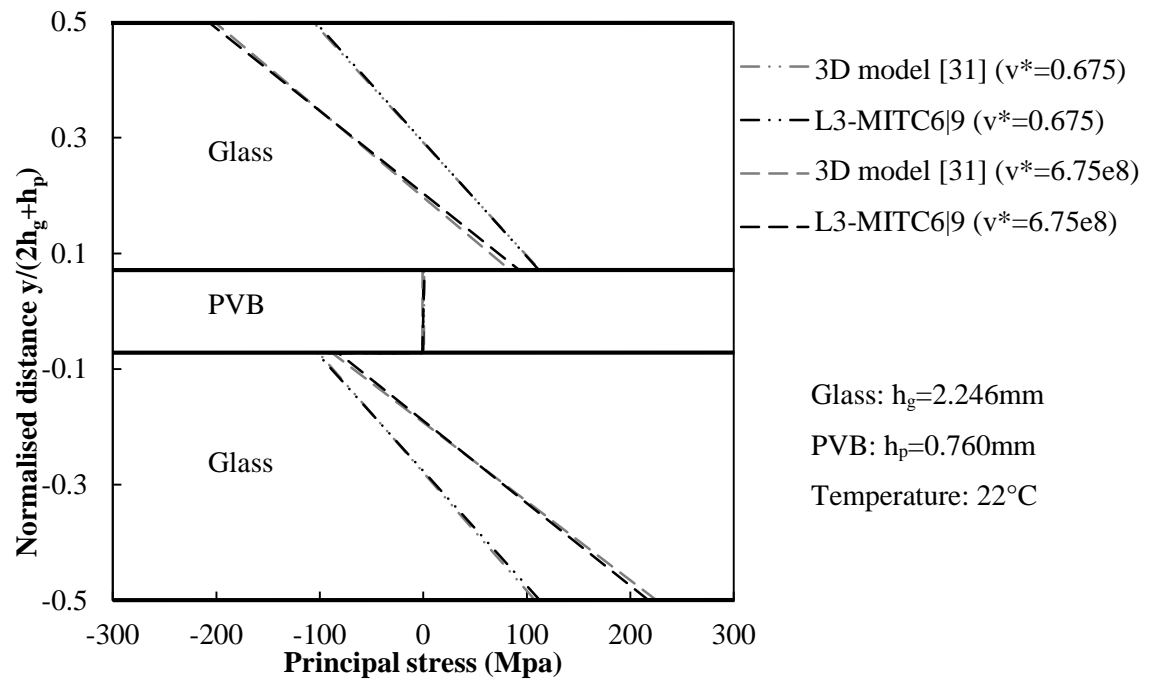
Figure 10: Distribution of normal stress for different loading rates.
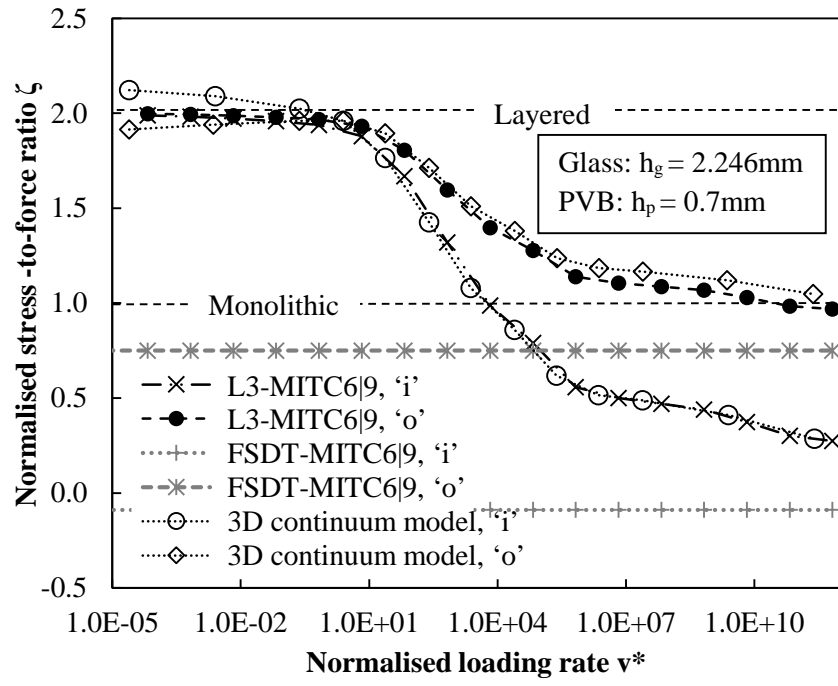
Figure 11: Normalised stress-to-force ratios with various loading rates.

a. Apple Store Fifth Avenue New York.
(www.idesignarch.com).
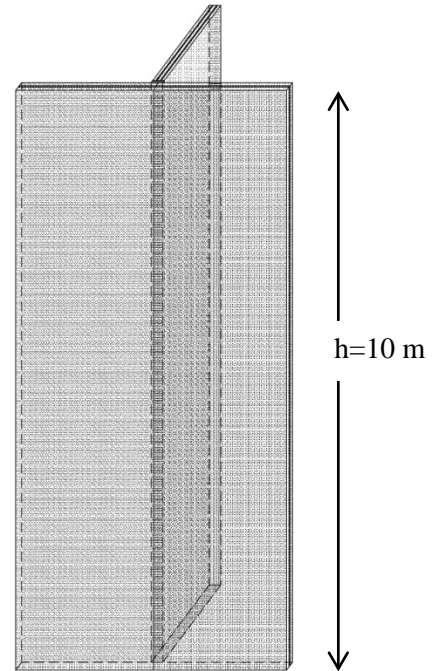
b. A partial model extracted from structure.

Figure 12: A LG structure.
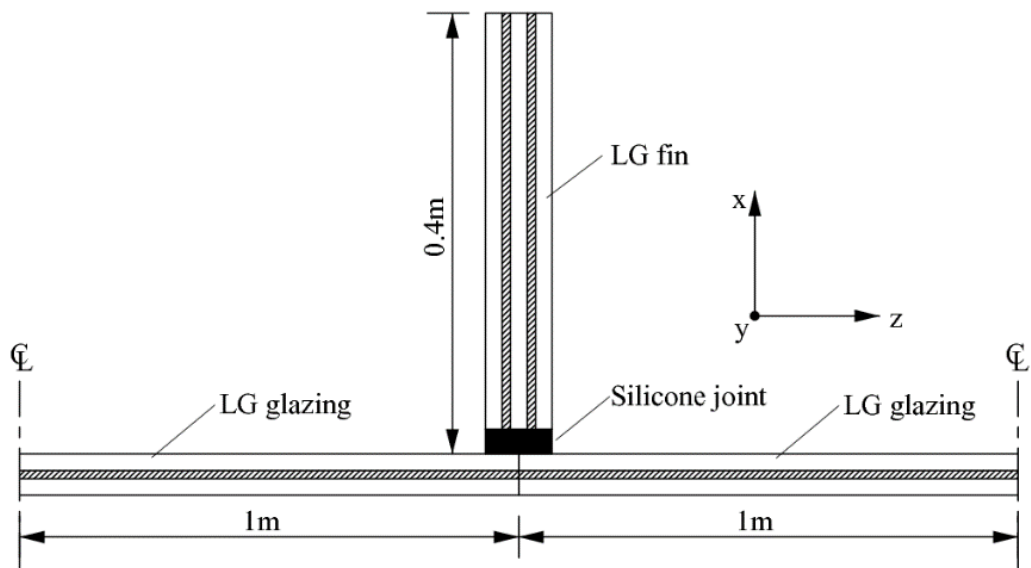
Figure 13: Plan view of the partial LG structure.
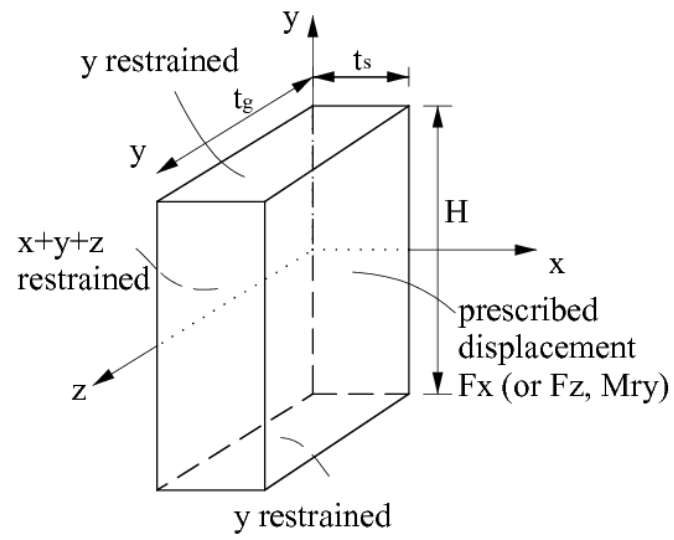
Figure 14: Boundary conditions for the silicone joint model.
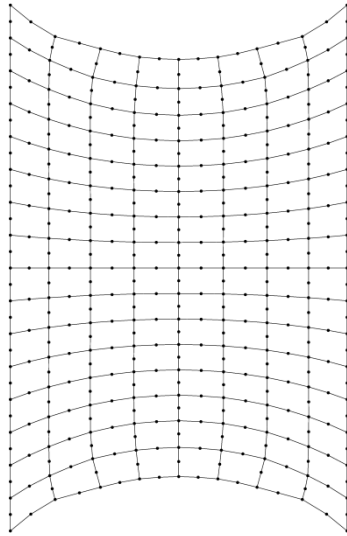
a. Deformation mode for a uniform elongation.
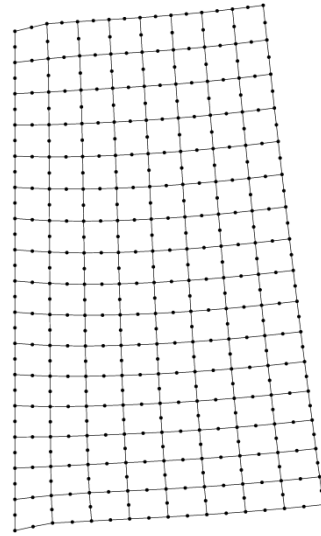
b. Deformation mode for a uniform rotation.

Figure 15: Representative cross-sectional deformation modes of silicone joint.

x+z restrained along the edge

Spring elements along
the vertical edge

x+z restrained along the edge

x+z restrained along the edge

z+ry

Weather seal

z+ry

A

x+z restrained
along the edge

y

y

y

y

x

z

x+z restrained along the edge

x+z restrained along the edge

Spring elements along
the vertical edge

A

x+z restrained
along the edge

y

y

x

z
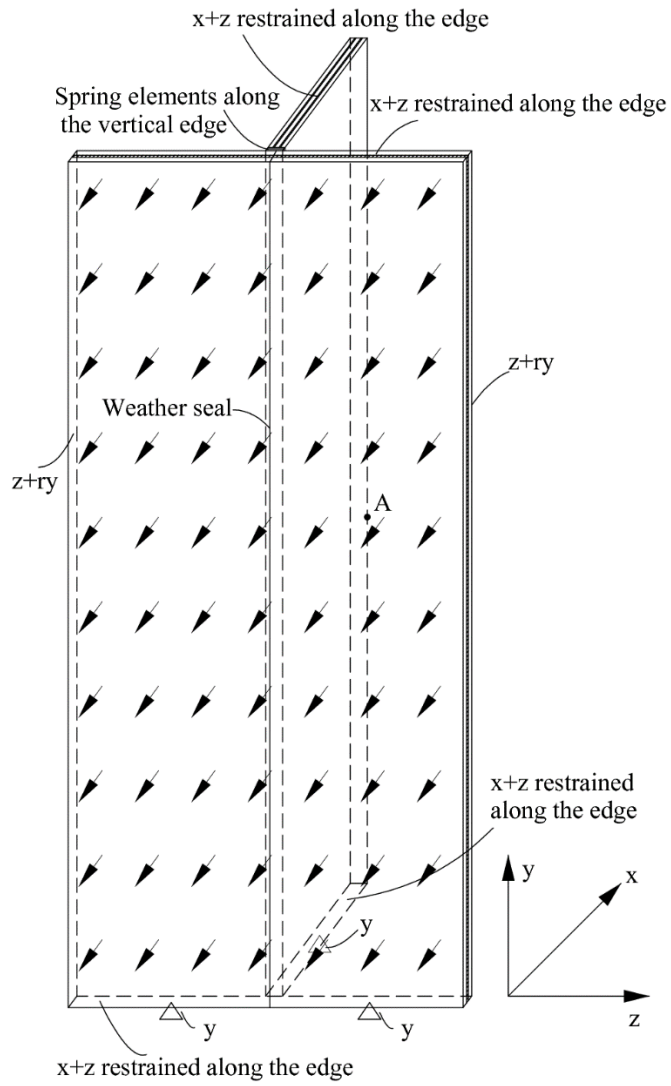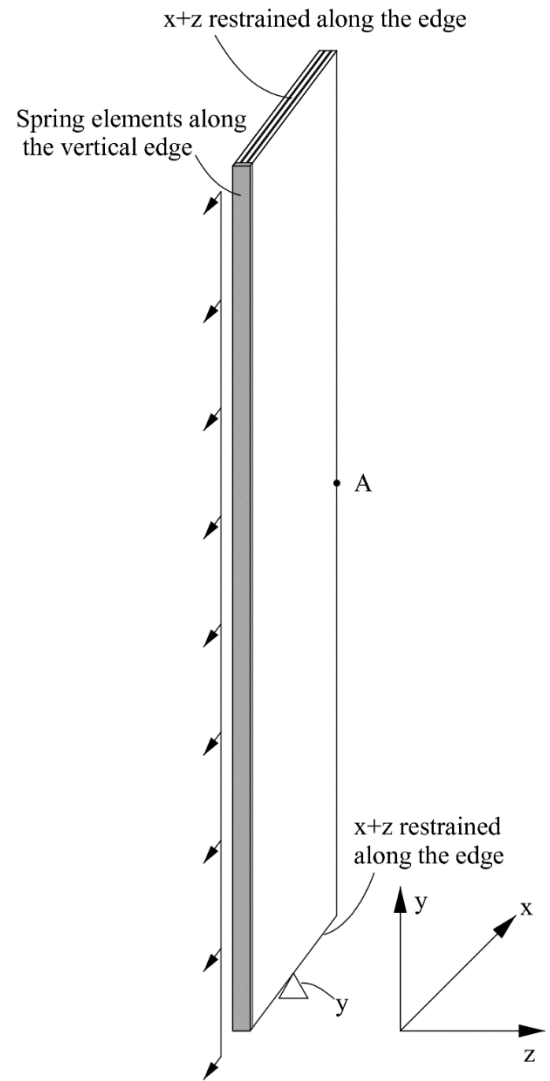
a. fin-glazing model

b. fin model

Figure 16: Boundary conditions for the fin-glazing model and the fin model.
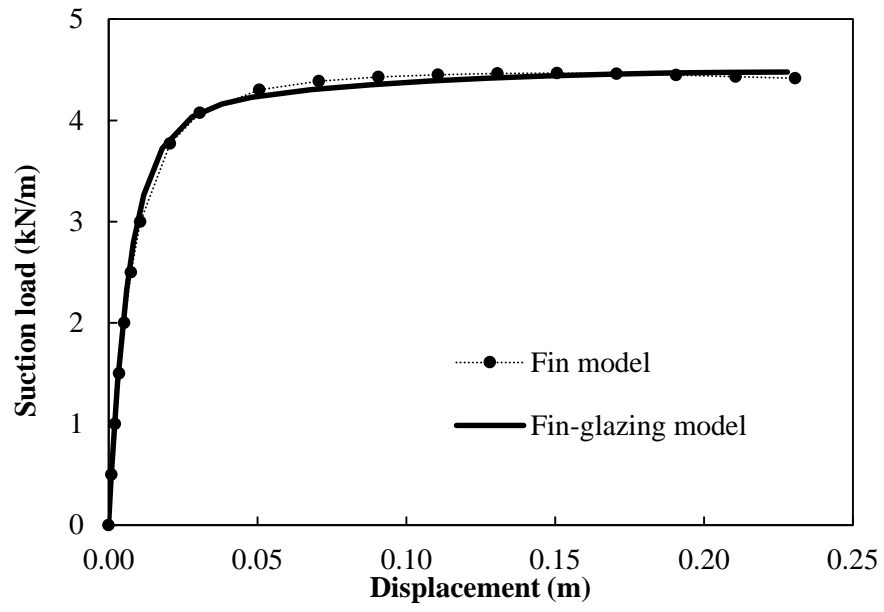
Figure 17: Load-displacement curves of the fin-glazing model and the fin model.
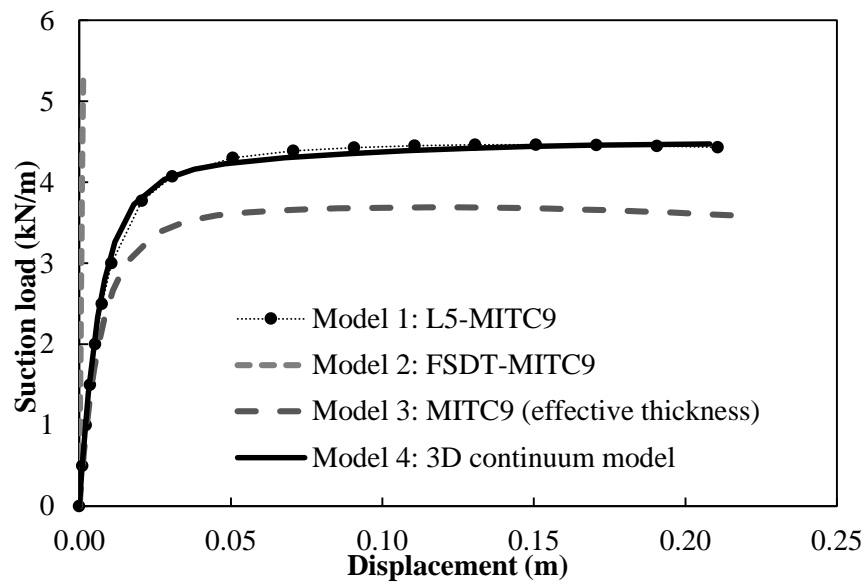
Figure 18: Load-displacement curves at point A for different models.
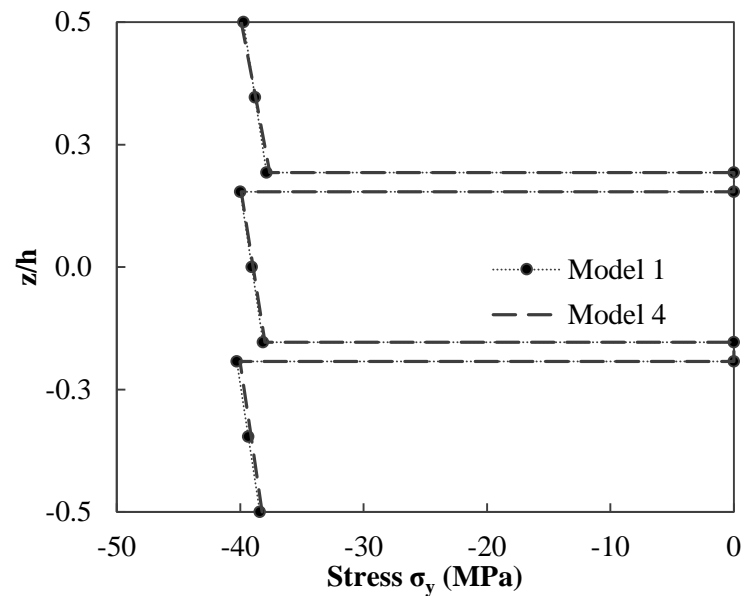
Figure 19: Through-thickness distribution of stress σ_y at point A for different models for a suction load of 3 kN/m.
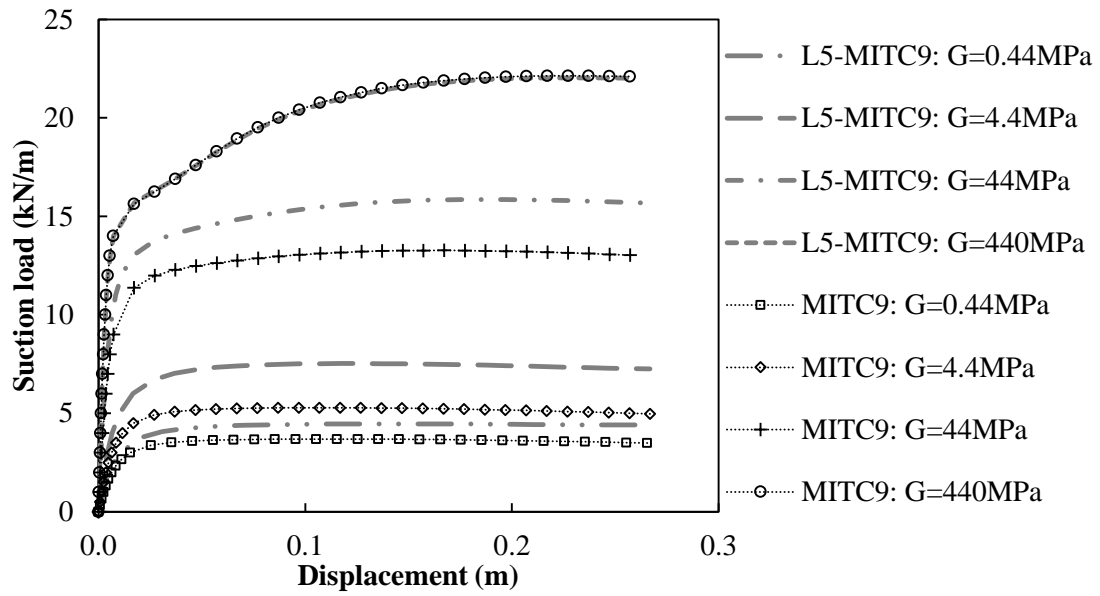
Figure 20: Load-displacement curves at point A with different PVB shear modulus (three-ply LG).
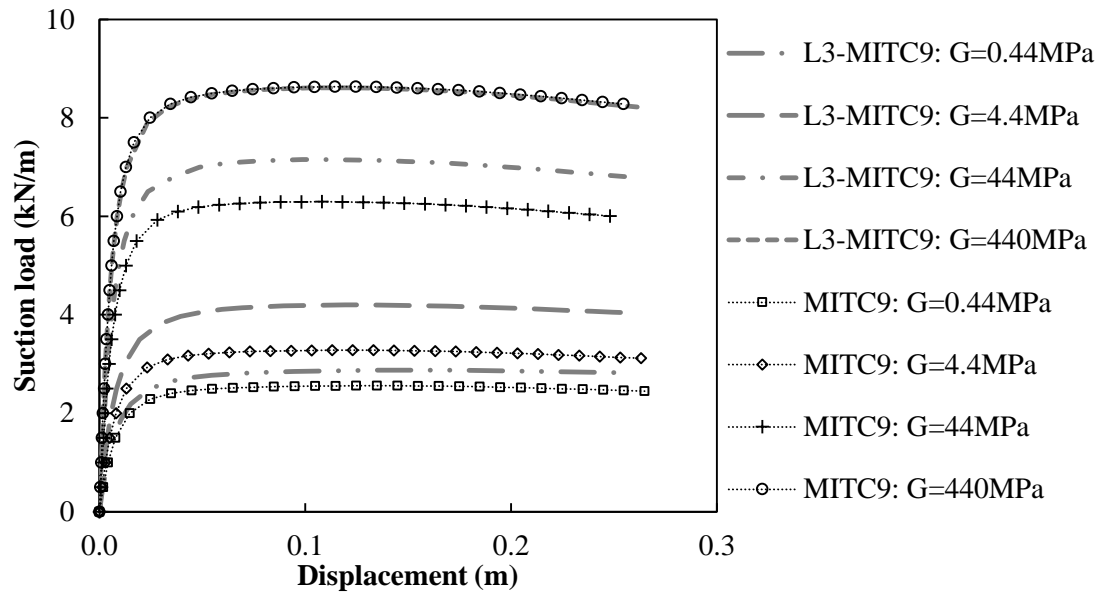
Figure 21: Load-displacement curves at point A with different PVB shear modulus (two-ply LG).
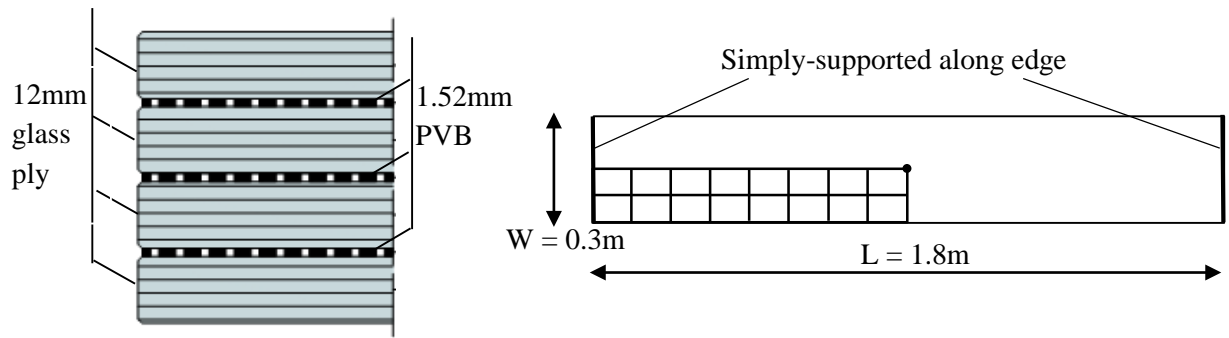
a. through-thickness representation.   b. shell model of the glass stair.

Figure 22: Geometric configuration and boundary conditions of the LG stair.
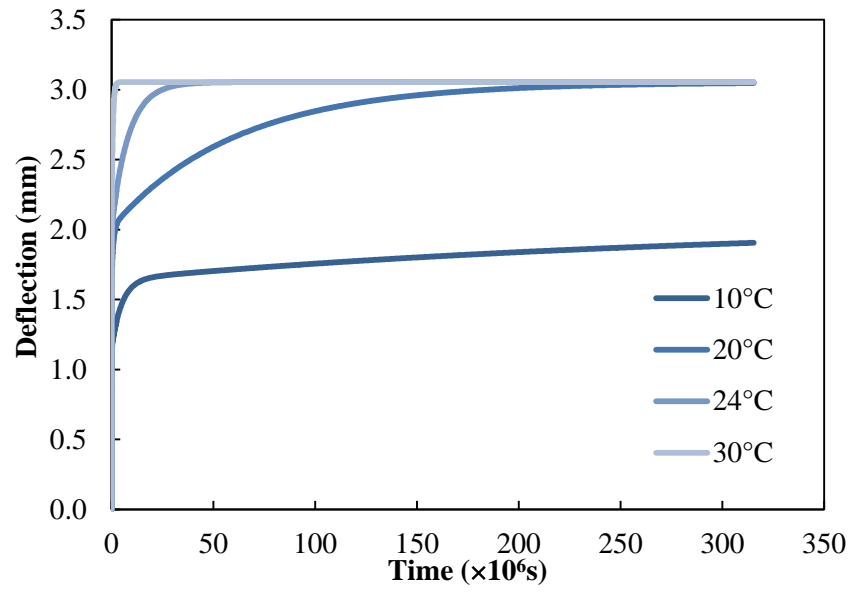
Figure 23: Influence of the temperature on the deflection time history.
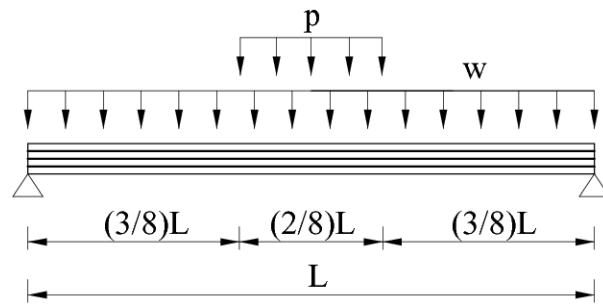
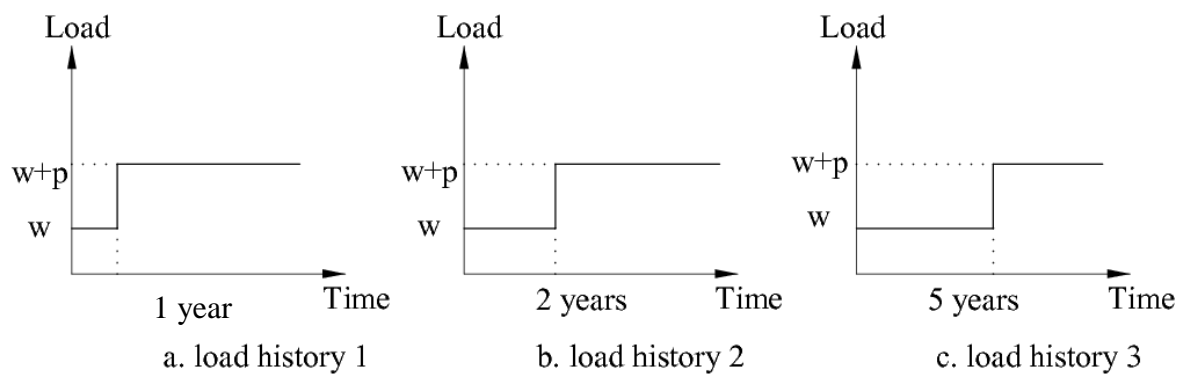Figure 24: Schematic representation of applied external loading.

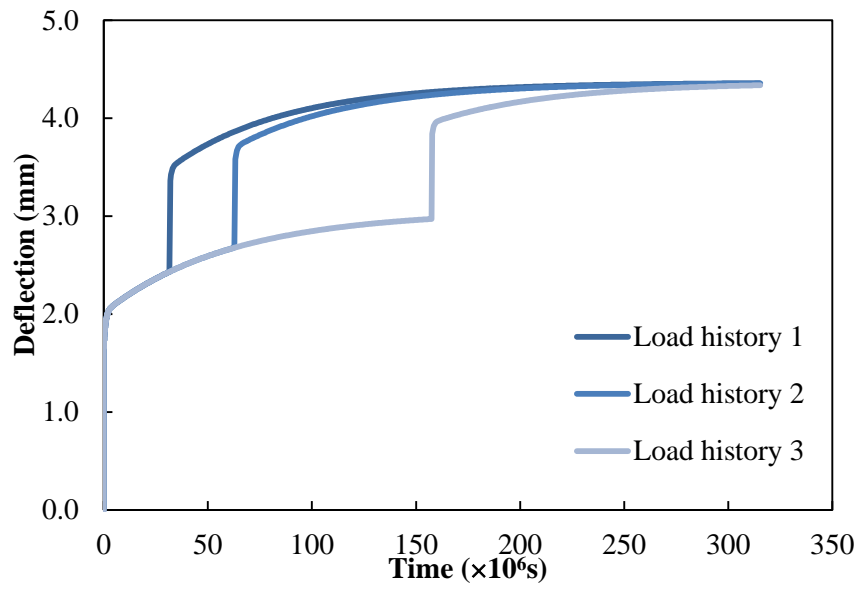Figure 25: Three load histories with different times of load application.

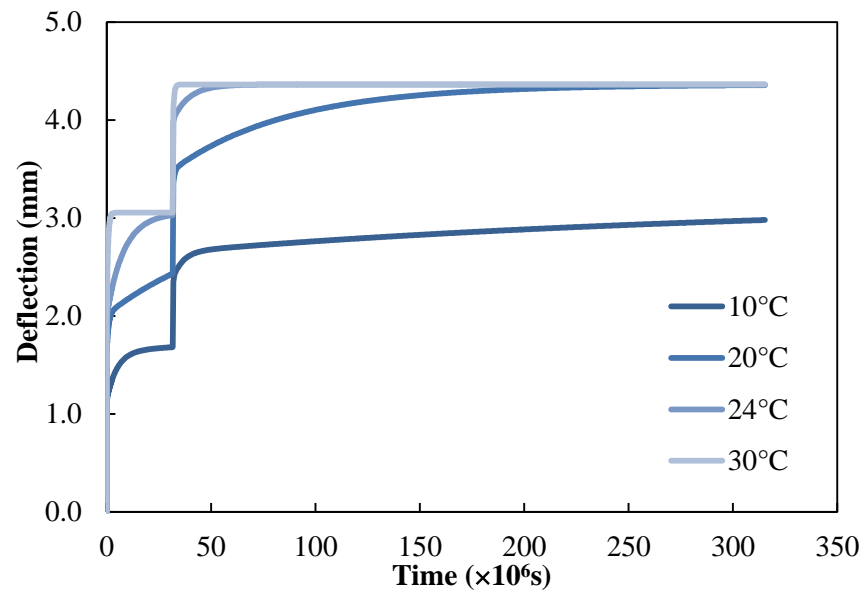Figure 26: Deflection time history of the LG stair with different time of loading.

Figure 27: Deflection time history of the LG stair with different operation temperatures.